Supporting information

Circularly Polarized Electroluminescence from Sterically Engineered Ruthenium(II) Complexes Enabled by a Chiral Anion Strategy in OLEDs

Jin-Yue Guo,[a,b] *Zhong-Qiu Li*,*[a,c] *Jian-Cheng Chen*,[a,b] *Yongli Yan*,*[a,b] *Yu-Wu Zhong*[a,b,c]*

Materials

All reagents were commercially available and used without further purification. Organic ligands were synthesized following literature procedures, [1,2] whereas 2,2'-bipyridine was obtained from commercial sources and used as received. The precursor complexes Ru1 and Ru2 were prepared using previously reported microwave-assisted methods. [3] The new complex Ru3 was synthesized under reflux conditions. The chiral ionic liquid (IL), 1-butyl-3-methylimidazolium 10-(+)/(−)-camphorsulfonate ([BMIM][(+)/(−)-CS]), was prepared via an ion-exchange reaction. The key intermediate, silver (+)/(−)-camphorsulfonate ((+)/(−)-AgCS), was first synthesized by reacting silver carbonate with (+)/(−)-camphorsulfonic acid.

Single-Crystal Growth of Ru3((+)-CS)$_2$ and Ru3((−)-CS)$_2$

Red needle-shaped single crystals of Ru3((+)-CS)$_2$ and Ru3((−)-CS)$_2$ suitable for X-ray diffraction were grown by vapor diffusion of diethyl ether into their acetonitrile (ACN) solutions (15 mg/mL).

Device Fabrication

ITO-coated glass substrates (anode) were sequentially cleaned by ultrasonication in detergent solution, deionized water, ethanol, acetone, and isopropanol for 20 min each. After drying under a nitrogen stream, the ITO substrates were treated with UV-ozone for 30 min.

LEC Fabrication: Poly(3,4-ethylenedioxythiophene):polystyrene sulfonate (PEDOT:PSS) was spin-coated onto the UV-ozone-treated ITO substrates at 4000 rpm for 30 s and subsequently annealed at 150 °C for 30 min. Subsequently, the emitting layer (EML) was prepared by spin-coating a solution (15 mg/mL in acetonitrile) of either Ru1((+)/(−)-CS)$_2$, Ru2((+)/(−)-CS)$_2$, or Ru3((+)/(−)-CS)$_2$, with or without the chiral IL, at 1500 rpm for 30 s, followed by annealing at 100 °C for 30 min. Finally, LiF (1 nm) and Al (~75 nm) were sequentially deposited by thermal evaporation under high vacuum (~1 × 10^{-5} Pa) as the electron-injection layer and cathode, respectively.

OLED Fabrication: PEDOT:PSS was spin-coated onto the UV-ozone-treated ITO substrates at 4000 rpm for 30 s as a hole-injection layer (HIL) and subsequently annealed at 150 °C for 30 min. Poly(9-vinylcarbazole) (PVK, 5 mg/mL in chlorobenzene) was spin-coated onto the PEDOT:PSS layer at 2000 rpm for 30 s to form the hole-transport layer (HTL) and annealed at 110 °C for 20 min. Subsequently, the EML of either Ru1((+)/(−)-CS)$_2$, Ru2((+)/(−)-CS)$_2$, or Ru3((+)/(−)-CS)$_2$, with or without the chiral IL (15 mg/mL in acetonitrile), was spin-coated onto PVK at 1500 rpm for 30 s and annealed at 100 °C for 30 min. Then, 1,3,5-tris(1-phenyl-1H-benzo[*d*]imidazol-2-yl)benzene (TPBi)

was deposited as an electron-transporting layer (40 nm) onto the EML under vacuum. Finally, LiF (1 nm) and Al (~75 nm) were successively deposited onto the TPBi layer.

Characterization

Structural and Photophysical characterization: ^{1}H and ^{13}C NMR spectra were recorded on a Bruker Avance 400 MHz spectrometer. High-resolution mass spectrometry (HRMS) data were obtained using a Bruker SolariX FTICR mass spectrometer equipped with a 9.4 T superconducting magnet. Single-crystal X-ray diffraction data were collected on a Rigaku XtaLAB Synergy-R diffractometer. UV–vis absorption and photoluminescence (PL) spectra, absolute fluorescence quantum yields, and excited-state lifetimes were measured using a TU-1810DSPC spectrophotometer, an F-380 spectrofluorimeter, a HORIBA FluoroMax+ spectrofluorimeter, and an FLS980 steady-state/transient fluorescence spectrometer, respectively. Circular dichroism (CD) and circularly polarized luminescence (CPL) spectra were recorded on JASCO J-1700 and JASCO CPL-200 spectrometers, respectively.

Electrochemical measurements: Cyclic voltammetry (CV) was performed on a CHI 660D potentiostat using a conventional three-electrode system consisting of a glassy carbon working electrode, a platinum wire counter electrode, and an Ag/AgCl reference electrode. Measurements were conducted in acetonitrile containing 0.1 M *n*-Bu_4NClO_4 as the supporting electrolyte at a scan rate of 100 $mV \cdot s^{-1}$. The analyte concentration was 1 mM, and potentials were referenced to the ferrocene/ferrocenium (Fc/Fc^{+}) redox couple.

Device characterization: Electroluminescence (EL) characteristics and current density–voltage–luminance (J–V–L) curves were simultaneously measured using a computer-controlled system comprising a Photo Research PR 750 luminance meter and a Keithley 2400 source meter. Circularly polarized electroluminescence (CPEL) spectra were recorded on a JASCO CPL-200 spectrometer. Film morphology and device cross-sections were characterized by atomic force microscopy (AFM, M8-HR) and scanning electron microscopy (SEM, Hitachi SU8010), respectively. All measurements were performed at room temperature unless otherwise specified.

Synthesis of ligands and Ru(II) complexes

Synthesis and characterization of Ligand 1

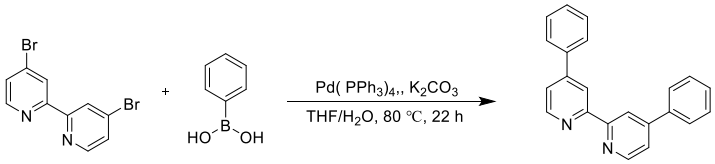

Ligand1

Known compound. A mixture of 4,4'-dibromo-2,2'-bipyridine (401.3 mg, 1.3 mmol), phenylboronic acid (370.5 mg, 3.0 mmol), K_2CO_3 (1.03 g, 7.5 mmol), and $Pd(PPh_3)_4$ (162.8 mg, 0.1 mmol) in THF/H_2O (2:1, v/v) was refluxed at 80 °C for 22 h under a nitrogen atmosphere. After cooling to room temperature, the THF was removed under reduced pressure. The aqueous residue was extracted with CH_2Cl_2 and washed with saturated NaCl solution. The crude product was purified by column chromatography (CH_2Cl_2/MeOH = 100:1, v/v) and recrystallized from a CH_2Cl_2/hexane mixture to afford Ligand 1 (248 mg, 63%) as a white solid. ^{1}H NMR (300 MHz, $CDCl_3$) δ 8.79–8.71 (m, 4H), 7.83–7.77 (m, 4H), 7.60–7.44 (m, 8H).

Synthesis and characterization of Ligand 2

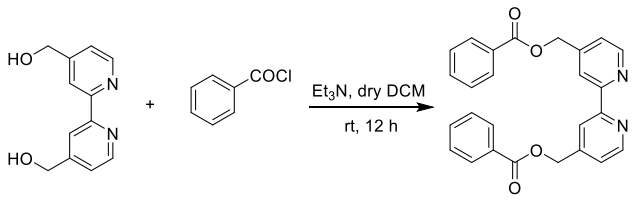

Ligand2

Known compound. A mixture of [2,2'-bipyridine]-4,4'-diyldimethanol (100.2 mg, 0.5 mmol), benzoyl chloride (0.3 mL, 2.5 mmol), and triethylamine (3 mL) in dry dichloromethane (30 mL) was stirred at room temperature for 12 h under a nitrogen atmosphere. The solvent was evaporated under reduced pressure, and the mixture was successively extracted with aqueous HCl, saturated aqueous $NaHCO_3$, and saturated aqueous NaCl. The crude product was purified by column chromatography (ethyl acetate) and then recrystallized from CH_2Cl_2/hexane to afford Ligand 2 (129 mg, 61%) as a white solid. ^{1}H NMR (400 MHz, $CDCl_3$) δ 8.70 (d, J = 5.0 Hz, 2H), 8.48 (s, 2H), 8.17–8.10 (m, 4H), 7.64–7.57 (m, 2H), 7.48 (t, J = 7.7 Hz, 4H), 7.41 (d, J = 5.0 Hz, 2H), 5.47 (s, 4H).

Synthesis and characterization of Ru (II) complexes

Synthesis of precursor complex Ru2

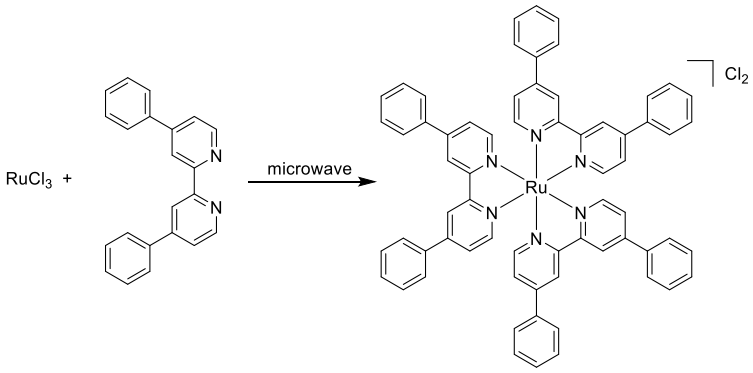

Ru2

Known compound. A mixture of ruthenium(III) trichloride (103.7 mg, 0.5 mmol) and 4,4'-diphenyl-2,2'-bipyridine (616.8 mg, 2.0 mmol) in ethylene glycol (3 mL) was refluxed for 20 min under microwave irradiation. After cooling to room temperature, the ethylene glycol was removed by extraction with CH_2Cl_2 and saturated aqueous NaCl. The crude product was purified by column chromatography (CH_2Cl_2/MeOH = 100:3, v/v) and then recrystallized from CH_2Cl_2/petroleum ether to afford complex Ru2 (481 mg, 88%) as a dark red solid. ^{1}H NMR (400 MHz, $CDCl_3$) δ 8.87 (d, J = 2.0 Hz, 6H), 8.17 (d, J = 6.0 Hz, 6H), 7.96 – 7.92 (m, 12H), 7.84 (dd, J = 6.0, 1.9 Hz, 6H), 7.58 – 7.48 (m, 18H). ESI-HRMS (P) calcd for $C_{66}H_{48}N_6Ru$ $[M–2Cl]^{2+}$: 513.1110. Found: 513.1494.

Synthesis of precursor complex Ru3

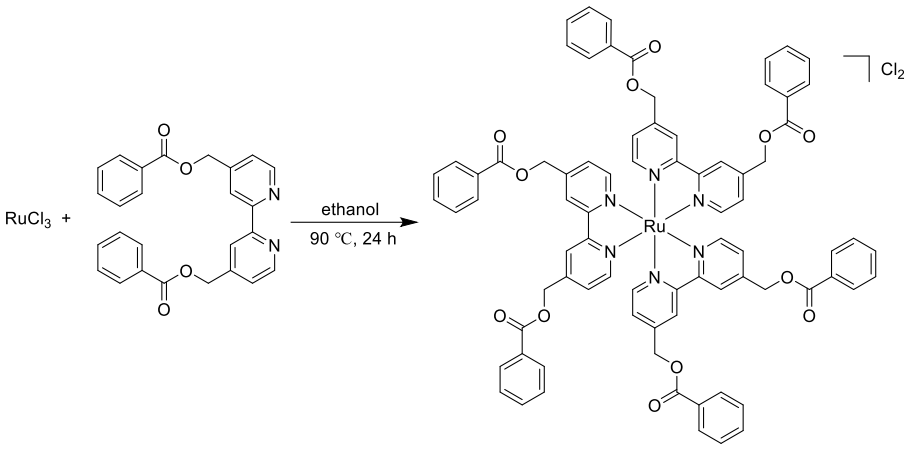

Ru3

A mixture of ruthenium(III) trichloride (84.6 mg, 0.4 mmol) and [2,2'-bipyridine]-4,4'-

diylbis(methylene) dibenzoate (1.13 g, 2.7 mmol) in ethanol (40 mL) was refluxed at 90 °C for 24 h under a nitrogen atmosphere. After cooling to room temperature, the solvent was removed on a rotary evaporator. The crude product was purified by column chromatography (CH_2Cl_2/MeOH = 50:3, v/v) and then recrystallized from CH_2Cl_2/diethyl ether to afford complex Ru3 (383.0 mg, 66%) as a red solid. ^{1}H NMR (400 MHz, $CDCl_3$) δ 8.79 (s, 6H), 8.04 – 8.01 (m, 12H), 7.91 (d, *J* = 5.6 Hz, 6H), 7.61 – 7.53 (m, 12H), 7.41 (t, *J* = 7.8 Hz, 12H), 5.61 (s, 12H). ESI-HRMS (P) calcd for $C_{78}H_{60}N_6O_{12}Ru$ $[M–2Cl]^{2+}$: 687.2190. Found: 687.1663.

Preparation and characterization of Ru1((+)-CS)$_2$ and Ru1((−)-CS)$_2$

A suspension of Ru1 (64.3 mg, 0.1 mmol) and (+)-AgCS (or (−)-AgCS) (67.9 mg, 0.2 mmol) in a mixture of MeOH (10 mL) and ACN (20 mL) was refluxed at 70 °C for 4 h under a nitrogen atmosphere. After cooling to room temperature, the precipitated AgCl was removed by filtration, and the solvent was evaporated under reduced pressure. The crude product was recrystallized from CH_2Cl_2/diethyl ether to afford Ru1((+)-CS)$_2$ (92.7 mg) as an orange-red solid in 90% yield, and Ru1((−)-CS)$_2$ (96.0 mg) in 93% yield, respectively. ^{1}H NMR (400 MHz, CD_3CN): *δ* 8.57 (d, *J* = 8.2 Hz, 6H), 8.06 (t, *J* = 7.9 Hz, 6H), 7.72 (d, *J* = 5.6 Hz, 6H), 7.39 (dd, *J* = 7.5, 5.6 Hz, 6H), 2.98 (dd, *J* = 14.5, 1.3 Hz, 2H), 2.82 – 2.74 (m, 2H), 2.50 (dd, *J* = 14.5, 1.4 Hz, 2H), 2.25 (dt, *J* = 18.2, 4.2 Hz, 2H), 1.96 (d, *J* = 5.8 Hz, 4H), 1.82 (s, 1H), 1.77 (s, 1H), 1.44 (ddd, *J* = 13.5, 9.2, 4.0 Hz, 2H), 1.34 – 1.28 (m, 2H), 1.09 (d, *J* = 1.4 Hz, 6H), 0.79 (s, 6H). ^{13}C NMR (100 MHz, CD_3CN): *δ* 217.36, 157.60, 152.18, 138.42, 128.14, 125.09, 117.90, 59.01, 47.84, 47.16, 43.13, 42.95, 27.15, 25.02, 20.15, 19.76. ESI-HRMS (P) calcd for $C_{30}H_{24}N_6Ru$ $[M–2CS]^{2+}$: 285.0551. Found: 285.0553. ESIHRMS (N) calcd for $[C_{10}H_{15}O_4S]^-$: 231.0697. Found: 231.0698.

Preparation and characterization of Ru2((+)-CS)$_2$ and Ru2((−)-CS)$_2$

A suspension of Ru2 (109.8 mg, 0.1 mmol) and (+)-AgCS (or (−)-AgCS) (68.0 mg, 0.2 mmol) in a mixture of MeOH (10 mL) and ACN (20 mL) was refluxed at 70 °C for 4 h under a nitrogen atmosphere. After cooling to room temperature, the precipitated AgCl was removed by filtration, and the solvent was evaporated under reduced pressure. The crude product was recrystallized from CH_2Cl_2/diethyl ether to afford Ru2((+)-CS)$_2$ (135.7 mg, 91% yield) as a dark red solid. Ru2((−)-CS)$_2$ was obtained similarly (132.3 mg, 89% yield). ^{1}H NMR (400 MHz, $CDCl_3$) *δ* 9.04 (s, 6H), 7.99 (dd, *J* = 10.4, 6.7 Hz, 18H), 7.78 (d, *J* = 6.0 Hz, 6H), 7.62 (dd, *J* = 10.5, 7.0 Hz, 18H), 3.00 (d, *J* = 14.6 Hz, 2H), 2.82 – 2.73 (m, 2H), 2.51 (d, *J* = 14.6 Hz, 2H), 2.27 (d, *J* = 4.1 Hz, 2H), 1.92 (dd, *J* = 7.8, 3.9 Hz, 2H), 1.80 (d, *J* = 18.0 Hz, 2H), 1.45 (td, *J* = 10.7, 5.9 Hz, 2H), 1.29 (t, *J* = 10.7 Hz, 4H), 1.09 (s, 6H), 0.79 (s, 6H).^{13}C NMR (100 MHz, CD_3CN): *δ* 217.48, 158.14, 152.30, 150.11, 136.35, 131.04, 130.03, 128.19, 125.62, 122.78, 117.91, 59.02, 47.84, 47.17, 43.12, 42.94, 27.13, 25.04 , 20.12, 19.74. ESI-HRMS (P) calcd for $C_{66}H_{48}N_6Ru$ $[M–2CS]^{2+}$: 513.1110. Found: 513.1494. ESIHRMS (N) calcd for

$[C_{10}H_{15}O_4S]^-$: 231.0697. Found: 231.0698.

Preparation and characterization of Ru3((+)-CS)$_2$ and Ru3((−)-CS)$_2$

A suspension of Ru3 (152.6 mg, 0.10 mmol) and (+)-AgCS (or (−)-AgCS) (70.8 mg, 0.20 mmol) in a mixture of CH_2Cl_2 (10 mL) and ACN (20 mL) was refluxed at 40 °C for 4 h under a nitrogen atmosphere. After cooling to room temperature, the precipitated AgCl was removed by filtration, and the solvent was evaporated under reduced pressure. The crude product was recrystallized from ACN/diethyl ether to afford Ru3((+)-CS)$_2$ (167.0 mg, 91% yield) as needle-like crystals. Ru3((−)-CS)$_2$ was obtained similarly (153.0 mg, 83% yield). ^{1}H NMR (400 MHz, CD_3CN) δ 8.70 (s, 6H), 8.11 – 8.01 (m, 12H), 7.75 (d, *J* = 5.8 Hz, 6H), 7.70 – 7.61 (m, 6H), 7.54 – 7.46 (m, 18H), 5.54 (s, 12H), 2.99 (d, *J* = 14.7 Hz, 2H), 2.81 – 2.71 (m, 2H), 2.50 (d, *J* = 14.6 Hz, 2H), 2.24 (t, *J* = 4.1 Hz, 2H), 1.92 – 1.85 (m, 2H), 1.77 (d, *J* = 18.0 Hz, 2H), 1.43 (ddd, *J* = 13.5, 9.1, 4.2 Hz, 2H), 1.26 (t, *J* = 10.5 Hz, 4H), 1.07 (s, 6H), 0.76 (s, 6H).^{13}C NMR (100 MHz, CD_3CN): δ 217.35, 166.31, 157.48, 152.27, 148.66, 134.18, 130.10, 129.30, 126.37, 123.57, 117.90, 64.54, 58.99, 47.83, 47.19, 43.10, 42.92, 27.13, 25.03, 20.13, 19.74. ESI-HRMS (P) calcd for $C_{78}H_{60}N_6O_{12}Ru$ $[M–2CS]^{2+}$: 687.2190. Found: 687.1657. ESIHRMS (N) calcd for $[C_{10}H_{15}O_4S]^-$: 231.0697. Found: 231.0693.

Supplementary Figures and Tables

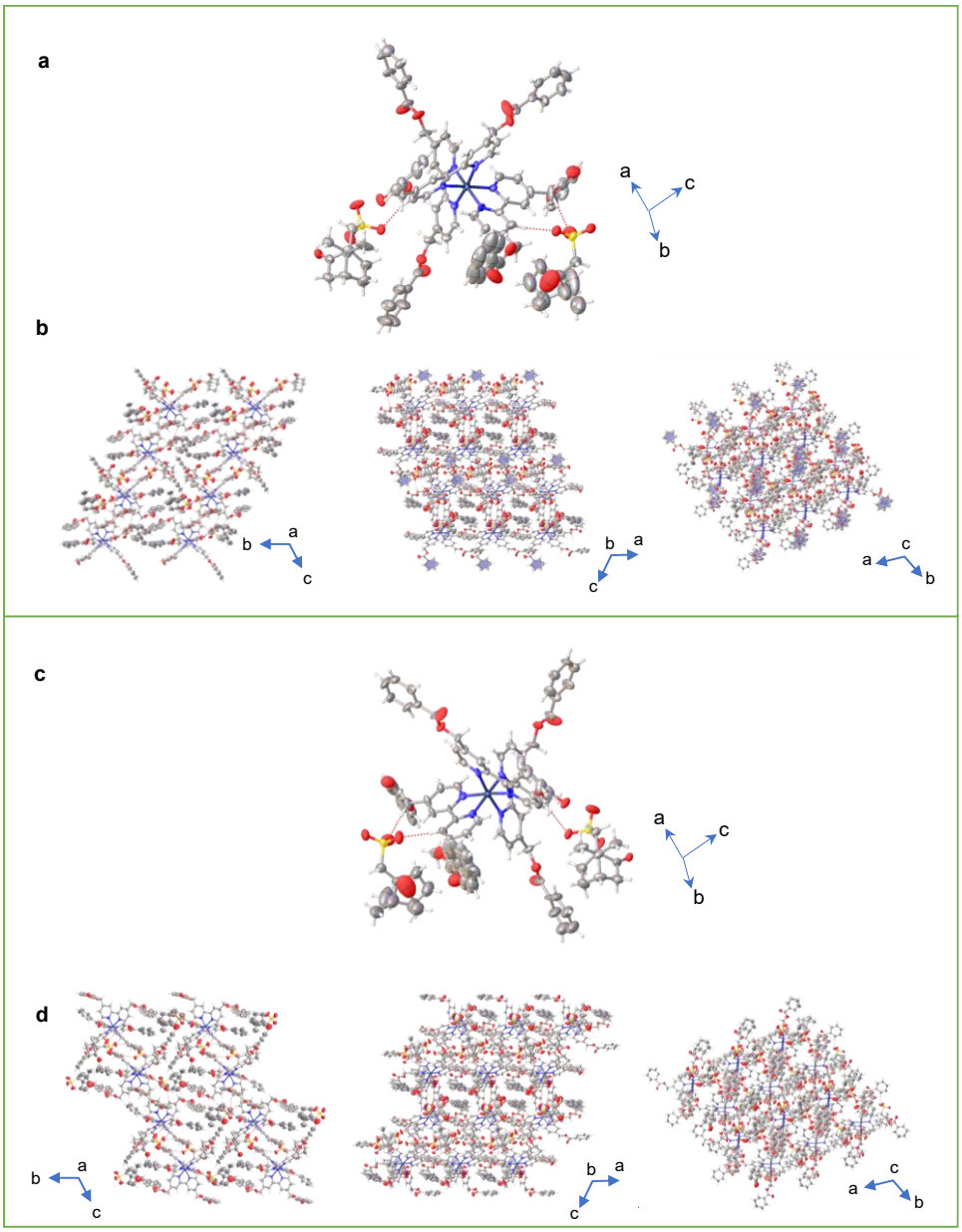

Fig. S1 Single-crystal structures. Thermal ellipsoid plot at 30% probability of the single-crystal structures of (a) Ru3((+)-CS)$_2$ and (c) Ru3((−)-CS)$_2$. (b, d) Crystal packing viewed from the axis (left), b axis (middle) and c axis (right) of (b) Ru3((+)-CS)$_2$ and (d) Ru3((−)-CS)$_2$, respectively.

Table S1. Crystallographic data and parameters of Ru3((+)-CS)$_2$ and Ru3((−)-CS)$_2$.

Name	Ru3((+)-CS)$_2$	Ru3((−)-CS)$_2$
CCDC number	2543549	2543562
Chemical formula	$C_{98}H_{90}N_6O_{20}RuS_2$	$C_{98}H_{90}N_6O_{20}RuS_2$
Formula weight	1836.94	1836.94
Temperature/K	170.15	170.15
Crystal system	triclinic	triclinic
Space group	*P*1	*P*1
a/Å	12.5730(2)	12.5922(2)
b/Å	19.3811(2)	19.3693(3)
c/Å	22.1893(3)	22.2093(3)
A/°	112.1900(10)	112.2090(2)
β/°	102.3990(10)	102.4460(10)
γ/°	98.5660(10)	98.4640(10)
Volume/Å^3	4728.96(12)	4737.94(14)
Z	2	2
ρ_{calc} g/cm^3	1.290	1.288
Radiation	Cu Kα (λ = 1.54184)	Cu Kα (λ = 1.54178)
R1 (final)	0.0638	0.0718
wR2 (final)	0.1680	0.2064
R1 (all)	0.0768	0.0898
wR2 (all)	0.1799	0.2326
Flack parameter	0.123(10)	0.085(10)

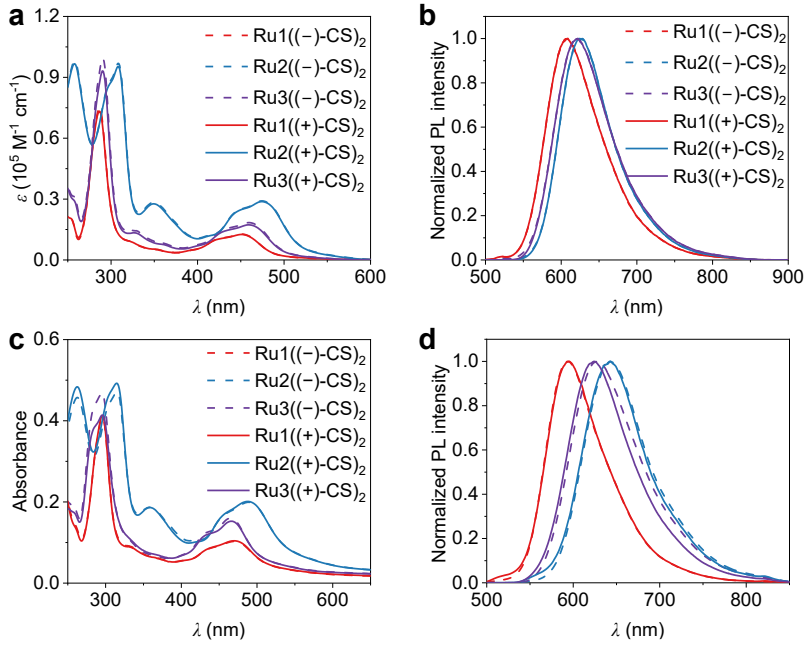

Fig. S2 (a, c) UV-vis absorption and (b, d) PL spectra of (a, b) solution (10^{-5} M in CH_3CN) and (c, d) spin-coated films (15 mg/mL) of Ru1((+)/(−)-CS)$_2$, Ru2((+)/(−)-CS)$_2$ and Ru3((+)/(−)-CS)$_2$.

Table S2. Photophysical data of spin-coated films.

film	λ_{ex} (nm)	λ_{em} (nm)	τ (ns)	Φ_{PL} (%)	k_r ($\times 10^6$ s^{-1})	k_{nr} ($\times 10^6$ s^{-1})
Ru1((−)-CS)$_2$	450	595	697	10.4	0.15	1.29
Ru1((+)-CS)$_2$	450	594	695	9.4	0.14	1.30
Ru2((−)-CS)$_2$	460	643	669	18.6	0.28	1.22
Ru2((+)-CS)$_2$	460	643	660	16.0	0.24	1.27
Ru3((−)-CS)$_2$	450	626	875	19.8	0.23	0.92
Ru3((+)-CS)$_2$	450	624	871	19.7	0.23	0.92

Table S3. Photophysical data of Ru1((+)/(−)-CS)$_2$, Ru2((+)/(−)-CS)$_2$ and Ru3((+)/(−)-CS)$_2$ in solution (10^{-5} M in CH_3CN). (Solutions were deoxygenated by argon bubbling for 10 min prior to measurement. Photoluminescence quantum yields and emission lifetimes were recorded in sealed cuvettes under an inert atmosphere.)

solution	λ_{ex} (nm)	λ_{em} (nm)	τ (ns)	Φ_{PL} (%)	k_r ($\times 10^6$ s^{-1})	k_{nr} ($\times 10^6$ s^{-1})
Ru1((−)-CS)$_2$	450	607	509	9.2	0.18	1.78
Ru1((+)-CS)$_2$	450	606	450	9.8	0.22	2.00
Ru2((−)-CS)$_2$	460	626	526	14.7	0.28	1.62
Ru2((+)-CS)$_2$	460	626	567	14.9	0.26	1.50
Ru3((−)-CS)$_2$	450	620	567	17.4	0.31	1.45
Ru3((+)-CS)$_2$	450	620	534	18.9	0.35	1.52

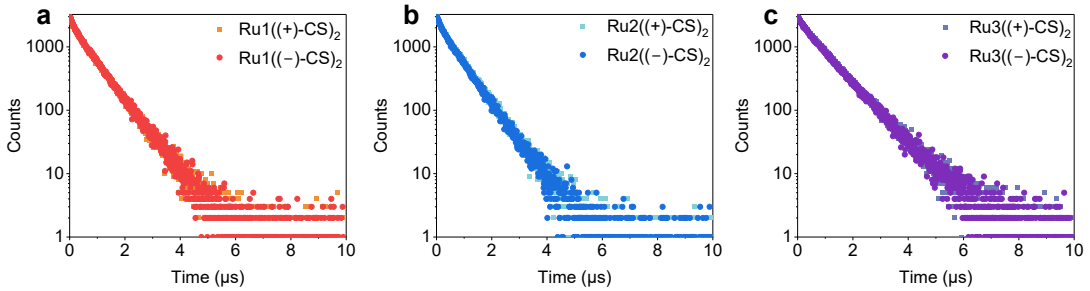

Fig. S3 Lifetime decays of spin-coated films (15 mg/mL) of (a) Ru1((+)/(−)-CS)$_2$, (b) Ru2((+)/(−)-CS)$_2$ and (c) Ru3((+)/(−)-CS)$_2$.

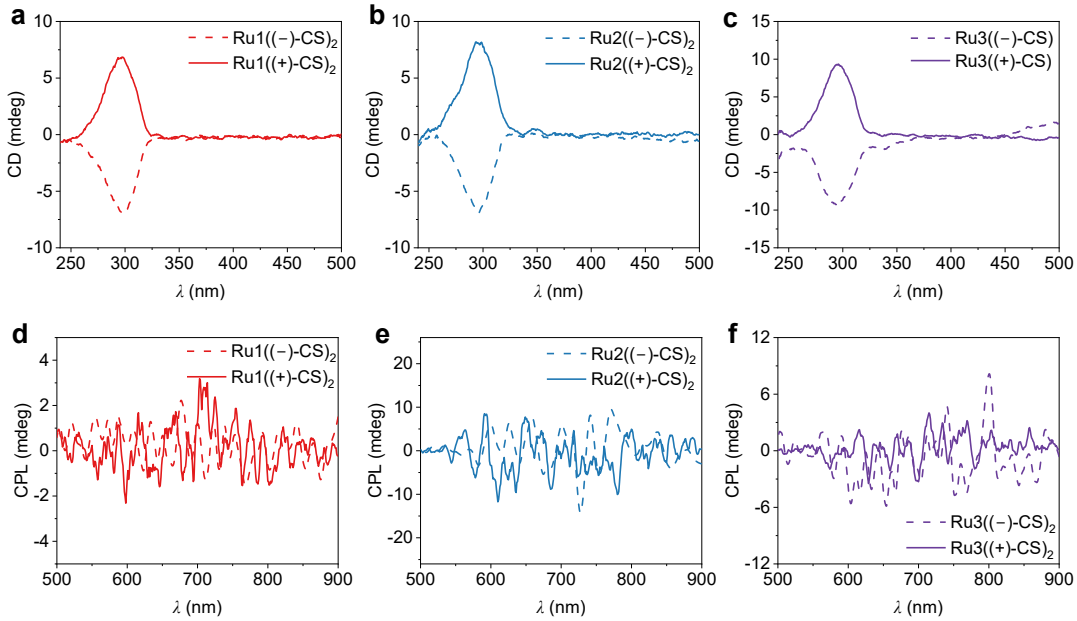

Fig. S4 (a–c) CD and (d–f) CPL spectra of (a, d) Ru1((+)/(−)-CS)$_2$, (b, e) Ru2((+)/(−)-CS)$_2$ and (c, f) Ru3((+)/(−)-CS)$_2$ in CH_3CN (10^{-5} M).

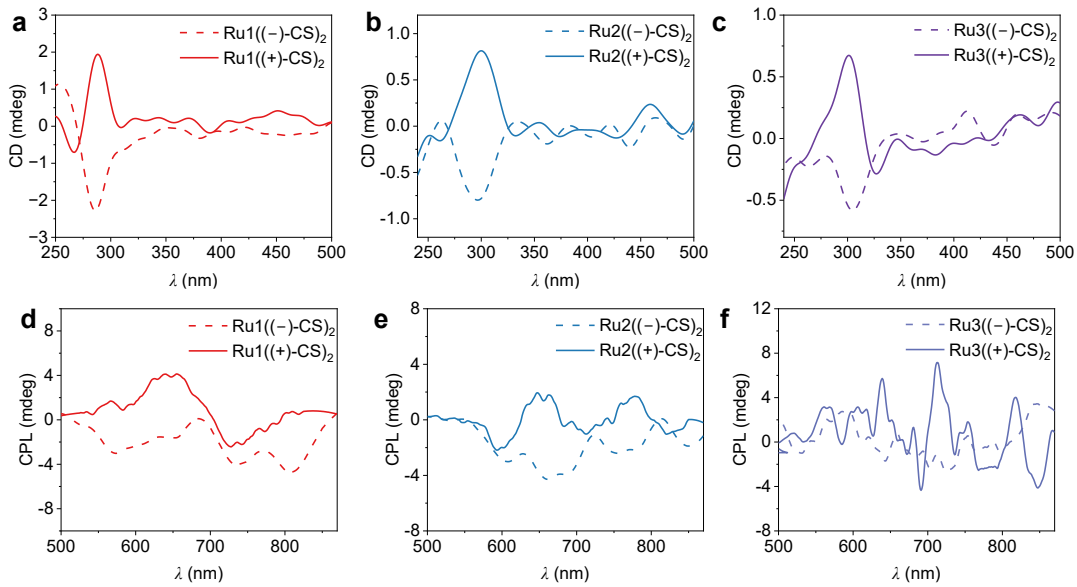

Fig. S5 (a–c) CD spectra and (d–f) CPL spectra of spin-coated films (15 mg/mL) of (a, d) Ru1((+)/(−)-CS)$_2$, (b, e) Ru2((+)/(−)-CS)$_2$ and (c, f) Ru3((+)/(−)-CS)$_2$.

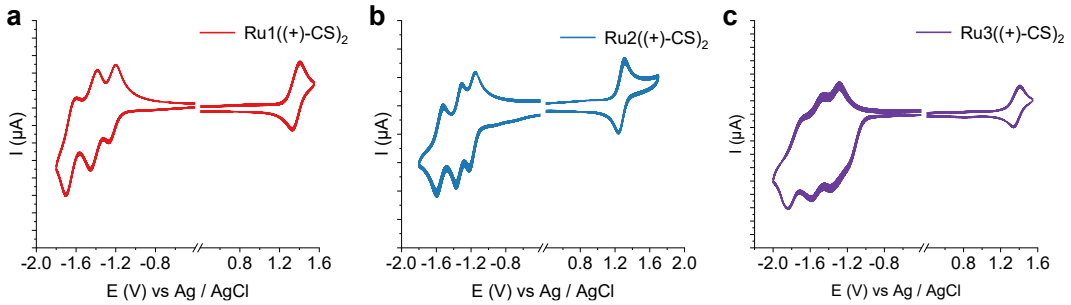

Fig. S6 Cyclic voltammetry (CV) curves (100 mV/s) of (a) Ru1((+)-CS)$_2$ (b) Ru2((+)-CS)$_2$ and (c) Ru3((+)-CS)$_2$. The electrolyte solution is 0.1 M *n*-Bu_4NClO_4/CH_3CN. The complexes with (−)-CS^- anions display the same electrochemical features.

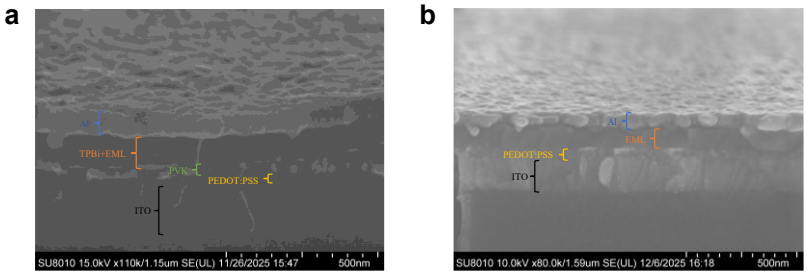

Fig. S7 The cross-section SEM images of (a) OLED and (b) LEC devices with Ru3((+)-CS)$_2$.

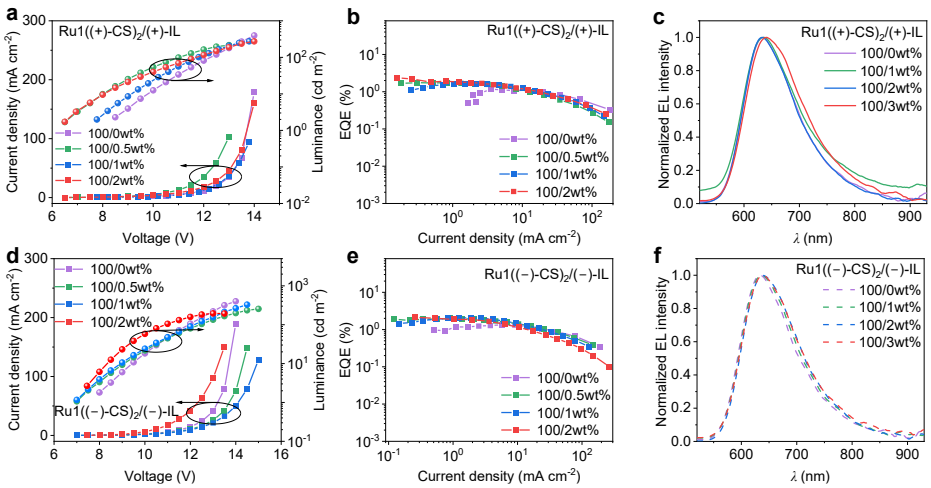

Fig. S8 Device performances of CP-OLEDs based on mixed Ru1((+)-CS)$_2$/(+)-IL or mixed Ru1((−)-CS)$_2$/(−)-IL with various weight ratios of Ru1((+)/(−)-CS)$_2$ vs (+)/(−)-IL. (a, d) current density-voltage-luminance curves; (b, e) EQE-current density curves; (c, f) EL spectra of (a–c) Ru1((+)-CS)$_2$ and (d–f) Ru1((−)-CS)$_2$ in the absence or presence of chiral ILs (the weight ratios of iTMCs/IL are indicated).

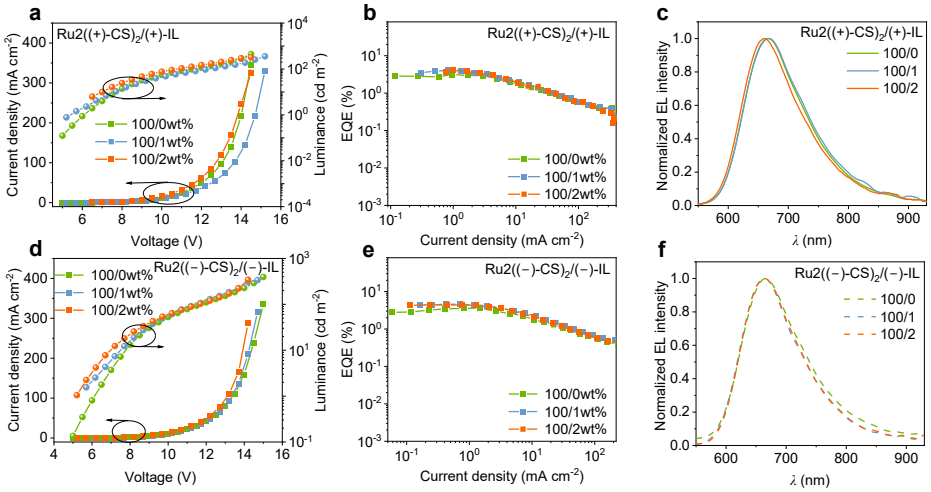

Fig. S9 Device performances of CP-OLEDs based on mixed Ru2((+)-CS)$_2$/(+)-IL or mixed Ru2((−)-CS)$_2$/(−)-IL with various weight ratios of Ru2((+)/(−)-CS)$_2$ vs (+)/(−)-IL. (a, d) current density-voltage-luminance curves; (b, e) EQE-current density curves; (c, f) EL spectra of (a–c) Ru2((+)-CS)$_2$ and (d–f) Ru2((−)-CS)$_2$ in the absence or presence of chiral ILs (the weight ratios of iTMCs/IL are indicated).

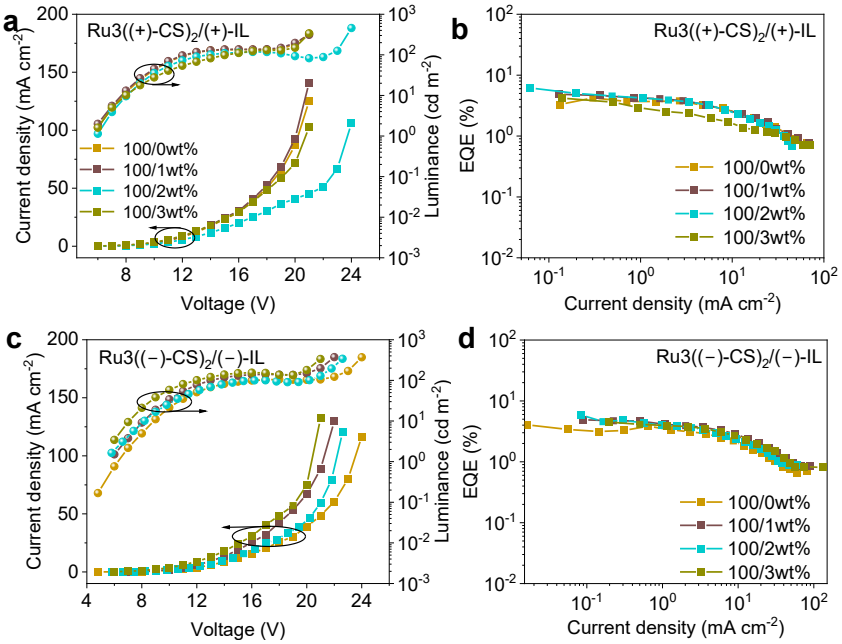

Fig. S10 Device performances of CP-OLEDs based on mixed Ru3((+)-CS)$_2$/(+)-IL or mixed Ru3((−)-CS)$_2$/(−)-IL with various weight ratios of Ru3((+)/(−)-CS)$_2$ vs (+)/(−)-IL. (a, c) current density-voltage-luminance curves; (b, d) EQE-current density curves of (a, b) Ru3((+)-CS)$_2$ and (c, d) Ru3((−)-CS)$_2$ in the absence or presence of chiral ILs (the weight ratios of iTMCs/IL are indicated).

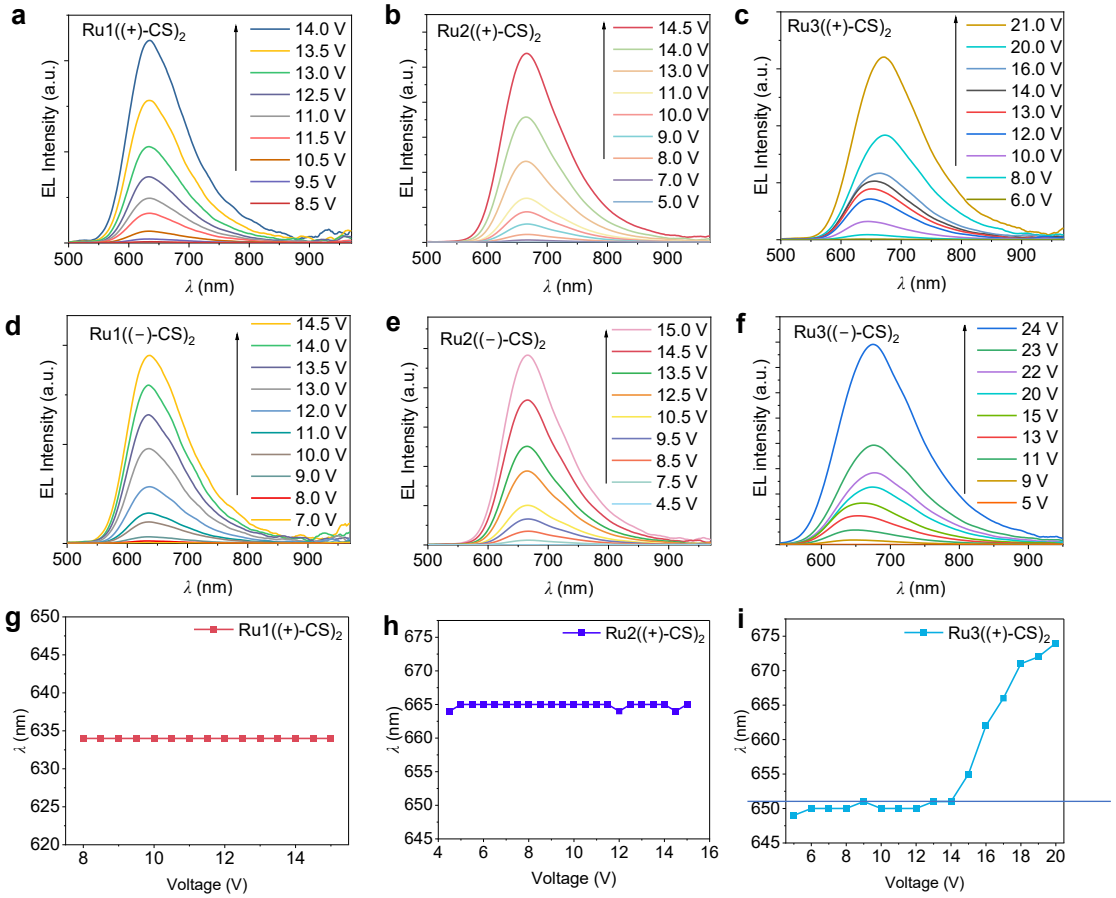

Fig. S11 (a–f) EL spectra of the OLEDs based on (a) Ru1((+)-CS)$_2$, (b) Ru2((+)-CS)$_2$, (c) Ru3((+)-CS)$_2$, (d)Ru1((−)-CS)$_2$, (e) Ru2((−)-CS)$_2$ and (f) Ru3((−)-CS)$_2$ driven at different pulsed voltages. (g–i) The corresponding EL peak wavelength as a function of applied voltage.

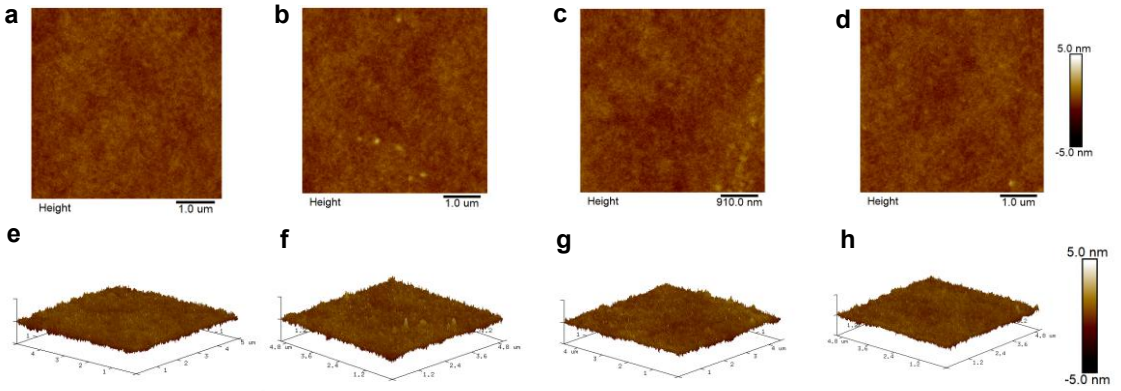

Fig. S12 Atomic force microscopy (AFM) images of OLED emissive layers (15 mg mL^{-1}) with weight ratios of Ru3((+)-CS)$_2$/(+)-IL of (a, e) 100:0, (b, f) 100:1, (c, g) 100:2, and (d, h) 100:3. (a–d) 2D height images and (e–h) corresponding 3D topography images. The root-mean-square (RMS) roughness values are 0.32, 0.33, 0.34, and 0.32 nm, respectively.

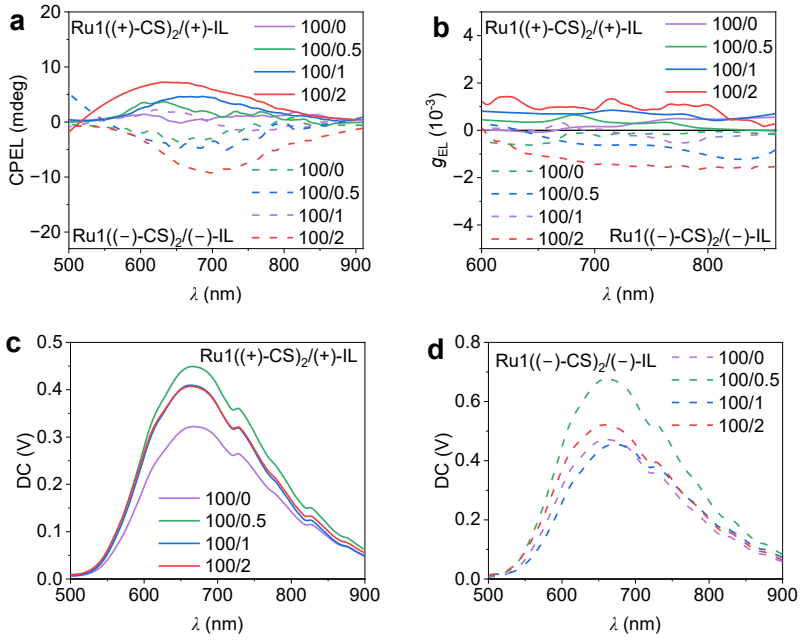

Fig. S13 CPEL performance of pristine and optimized CP-OLEDs with chiral ILs. (a) CPEL spectra of the OLEDs based on mixed Ru1((+)-CS)$_2$/(+)-IL or mixed Ru1((−)-CS)$_2$/(−)-IL with varying weight ratios of Ru1(CS)$_2$ vs IL. (b) g_{EL} versus wavelength of corresponding OLEDs. (c, d) EL spectra of corresponding CP-OLEDs.

Table S4. Key EL data of the CP-OLEDs based on mixed Ru1((+)-CS)$_2$/(+)-IL or mixed Ru1((−)-CS)$_2$/(−)-IL with various weight ratios of Ru1(CS)$_2$ vs IL. The g_{EL} values are expressed as mean ± error from three measurements.

EML	Weight ratio	CE_{max} (cd A^{-1})	L_{max} (cd m^{-2})	PE_{max} (lm W^{-1})	EQE_{max} (%)	λ_{EL}(nm)	g_{EL}
Ru1((+)-CS)$_2$/(+)-IL	100/0	0.70	396.4	0.20	1.20	634	-
	100/0.5	1.23	215.6	0.48	1.75	635	+3.0(±1.6) ×10^{-4}
	100/1	1.31	274.8	0.43	1.65	632	+6.7(±1.5) ×10^{-4}
	100/2	1.24	273.9	0.56	2.36	639	+1.1(±0.1) ×10^{-3}
Ru1((−)-CS)$_2$/(−)-IL	100/0	0.80	399.7	0.23	1.34	633	-
	100/0.5	1.19	327.9	0.44	1.98	637	−5.1(±1.0) ×10^{-4}
	100/1	1.19	254.8	0.40	2.08	638	−6.5(±1.9) ×10^{-4}
	100/2	1.23	195.0	0.46	2.12	638	−1.2(±0.2) ×10^{-3}

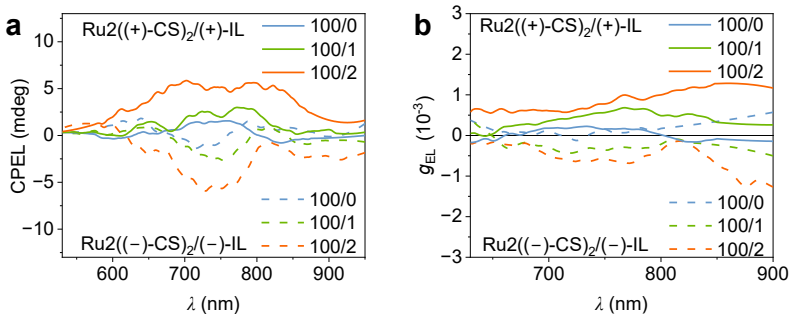

Fig. S14 CPEL performance of pristine and optimized CP-OLEDs with chiral ILs. (a) CPEL spectra of the OLEDs based on mixed Ru2((+)-CS)$_2$/(+)-IL or mixed Ru2((−)-CS)$_2$/(−)-IL with varying weight ratios of Ru2(CS)$_2$ vs IL. (b) g_{EL} versus wavelength of corresponding OLEDs.

Table S5. Key EL data of the CP-OLEDs based on mixed Ru2((+)-CS)$_2$/(+)-IL or mixed Ru2((−)-CS)$_2$/(−)-IL with various weight ratios of Ru2(CS)$_2$ vs IL. The g_{EL} values are expressed as mean ± error from three measurements.

EML	Weight ratio	CE_{max} (cd A^{-1})	L_{max} (cd m^{-2})	PE_{max} (lm W^{-1})	EQE_{max} (%)	λ_{EL}(nm)	g_{EL}
Ru2((+)-CS)$_2$/(+)-IL	100/0	0.80	445.2	0.38	3.14	667	-
	100/1	0.82	355.3	0.43	4.03	667	+2.1(±1.0) ×10^{-4}
	100/2	1.00	323.2	0.45	4.11	661	+6.7(±0.7) ×10^{-4}
	100/3	0.43	19.0	0.22	2.43	665	-
Ru2((−)-CS)$_2$/(−)-IL	100/0	0.90	394.9	0.40	3.61	665	-
	100/1	1.05	337.3	0.52	4.60	665	−3.1(±1.0) ×10^{-4}
	100/2	1.00	344.7	0.56	4.40	663	−6.6(±0.5) ×10^{-4}
	100/3	0.60	12.49	0.37	3.62	664	-

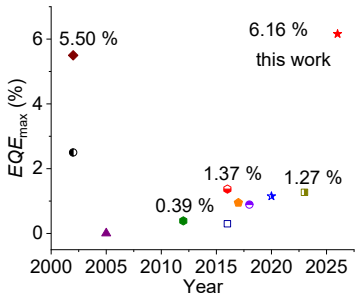

Fig. S15 The EQE_{max} of electroluminescent devices based on Ru (II) complexes.

Table S6. The electroluminescent devices based on Ru (II) complexes.

Year	Molecular structure	Device type	EQE_{max} (%)	Literature
2000	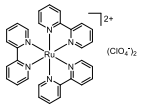	LEC	2.50	*J. Am. Chem. Soc.* **2000**, *122* (30), 7426–7427.
2002	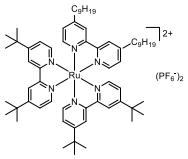	LEC	5.50	*J. Am. Chem. Soc.* **2002**, *124* (17), 4918–4921.
2008	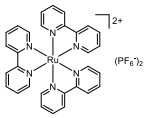	LEC	0.31	*Synth. Met.* **2008**, *158* (12), 484–488.
2009	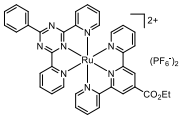	LEC	0.005	*Inorg. Chem.* **2009**, *48* (9), 3907–3909.
2012	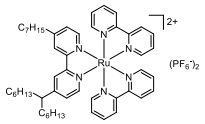	OLED	0.39	*Dyes Pigm.* **2012**, *95* (1), 23–32.
2016	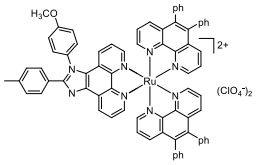	LEC	1.37	*J. Mater. Chem. C* **2016**, *4* (41), 9674–9679.
2017	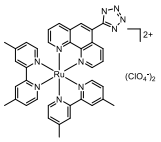	LEC	0.95	*Chem. Commun.* **2017**, *53* (46), 6211–6214.
2018	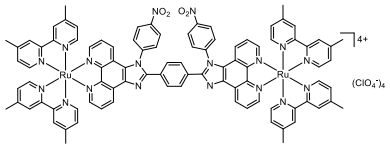	LEC	0.89	*Chem. Select* **2018**, *3* (25), 7226–7230.

2020	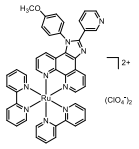	LEC	1.15	*New J. Chem.* **2020**, *44* (5), 1881–1887.
2023	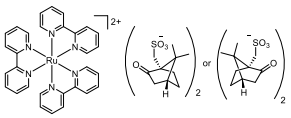	LEC	1.18,1.27	*Angew Chem Int Ed* **2023**, *62* (20), e202302160.

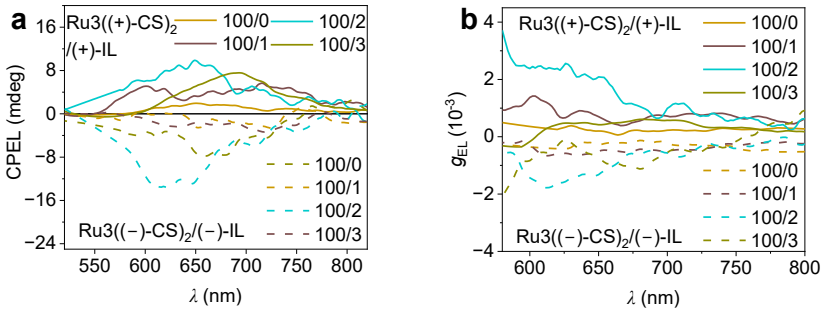

Fig. S16 CPEL performance of pristine and optimized CP-OLEDs with chiral ILs. (a) CPEL spectra of the OLEDs based on mixed Ru3((+)-CS)$_2$/(+)-IL or mixed Ru3((−)-CS)$_2$/(−)-IL with varying weight ratios of Ru3(CS)$_2$ vs IL. (b) g_{EL} versus wavelength of corresponding OLEDs.

Table S7. Key EL data of the CP-OLEDs based on mixed Ru3((+)-CS)$_2$/(+)-IL or mixed Ru3((−)-CS)$_2$/(−)-IL with various weight ratios of Ru3(CS)$_2$ vs IL. The g_{EL} values are expressed as mean ± error from three measurements.

EML	Weight ratio	CE_{max} (cd A^{-1})	L_{max} (cd m^{-2})	PE_{max} (lm W^{-1})	EQE_{max} (%)	λ_{EL}(nm)	g_{EL}
Ru3((+)-CS)$_2$/(+)-IL	100/0	1.70	332.2	0.66	4.22	648→674	+1.5(±0.4) ×10^{-4}
	100/1	1.64	311.1	0.82	4.86	646→670	+5.3(±1.0) ×10^{-4}
	100/2	1.95	457.4	0.95	6.16	647→666	+1.2(±0.2) ×10^{-3}
	100/3	1.16	336.9	0.61	4.20	648→667	+6.3(±0.5) ×10^{-4}
Ru3((−)-CS)$_2$/(−)-IL	100/0	1.70	370.9	0.71	4.05	647→671	−0.9(±0.4) ×10^{-4}
	100/1	1.83	372.8	0.90	4.90	647→671	−3.6(±0.7) ×10^{-4}
	100/2	2.00	340.3	1.10	5.90	648→671	−1.1(±0.1) ×10^{-3}
	100/3	1.89	335.5	0.91	4.48	648→669	−4.5(±1.2) ×10^{-4}

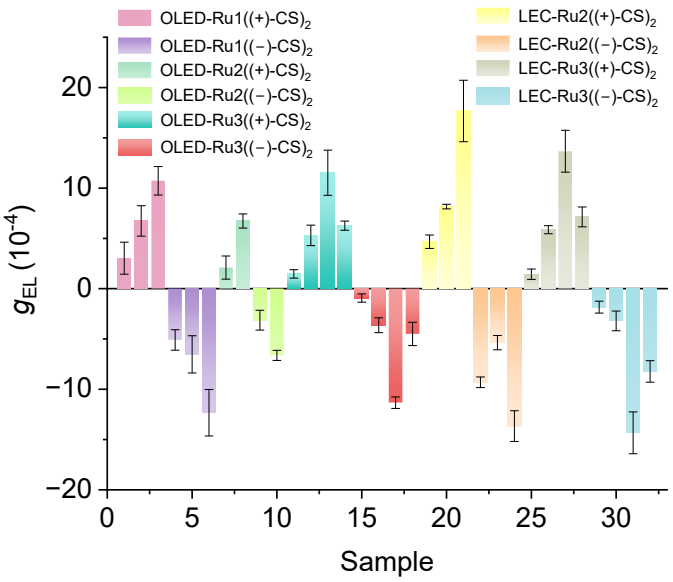

Fig. S17 Error bars represent the means ± standard deviation (SD) from three independent measurements (n = 3) under identical conditions. Each color corresponds to a specific molecule in OLED/LEC devices. For each color, bars from left to right represent increasing IL containing ratios where the g_{EL} first appears. Example: The first color (Ru1((+)-CS)$_2$) shows devices with weight ratios of 0.5 wt%, 1 wt%, and 2 wt% IL (left to right). The third color (Ru2((+)-CS)$_2$) shows devices with weight ratios of 1 wt% and 2 wt% IL.

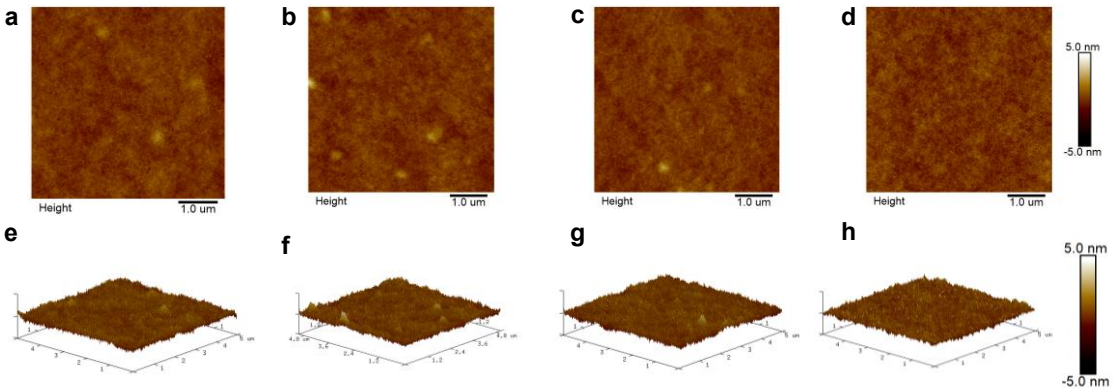

Fig. S18 Atomic force microscopy (AFM) images of LEC emissive layers (30 mg mL^{-1}) with molar ratios of Ru3((+)-CS)$_2$/(+)-IL of (a, e) 1:0, (b, f) 4:1, (c, g) 2:1, and (d, h) 1:1. (a–d) 2D height images and (e–h) corresponding 3D topography images. The root-mean-square (RMS) roughness values are 0.33, 0.34, 0.32, and 0.33 nm, respectively.

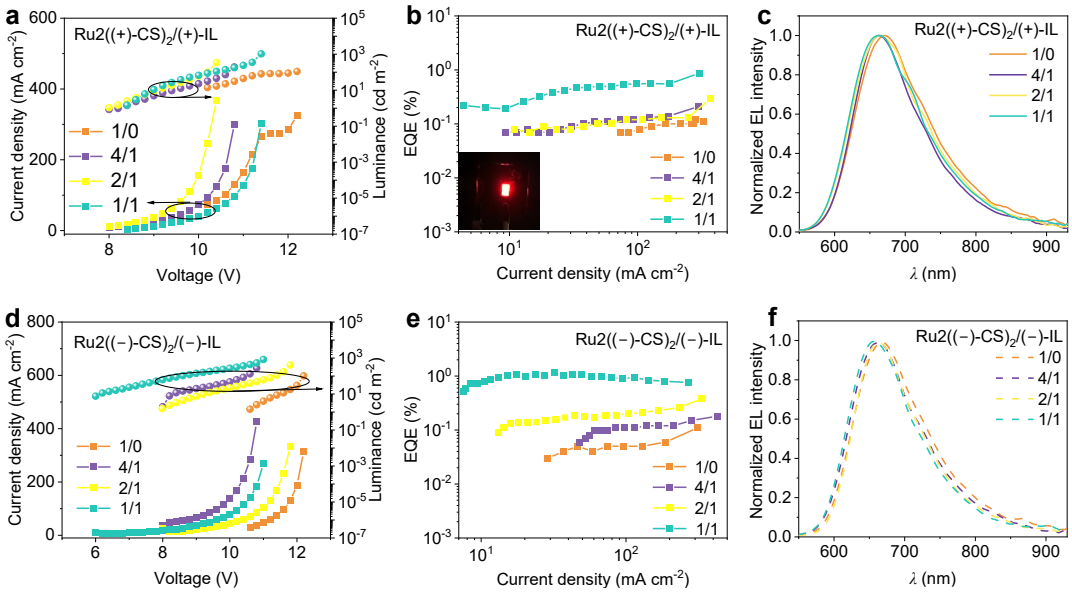

Fig. S19 Device performances of LECs based on mixed Ru2((+)-CS)$_2$/(+)-IL or mixed Ru2((−)-CS)$_2$/(−)-IL with various molar ratios of Ru2((+)/(−)-CS)$_2$ vs (+)/(−)-IL. (a, d) current density-voltage-luminance curves; (b, e) EQE-current density curves; (c, f) EL spectra of (a–c) Ru2((+)-CS)$_2$ and (d–f) Ru2((−)-CS)$_2$ in the absence or presence of chiral ILs (the molar ratios of iTMCs/IL are indicated).

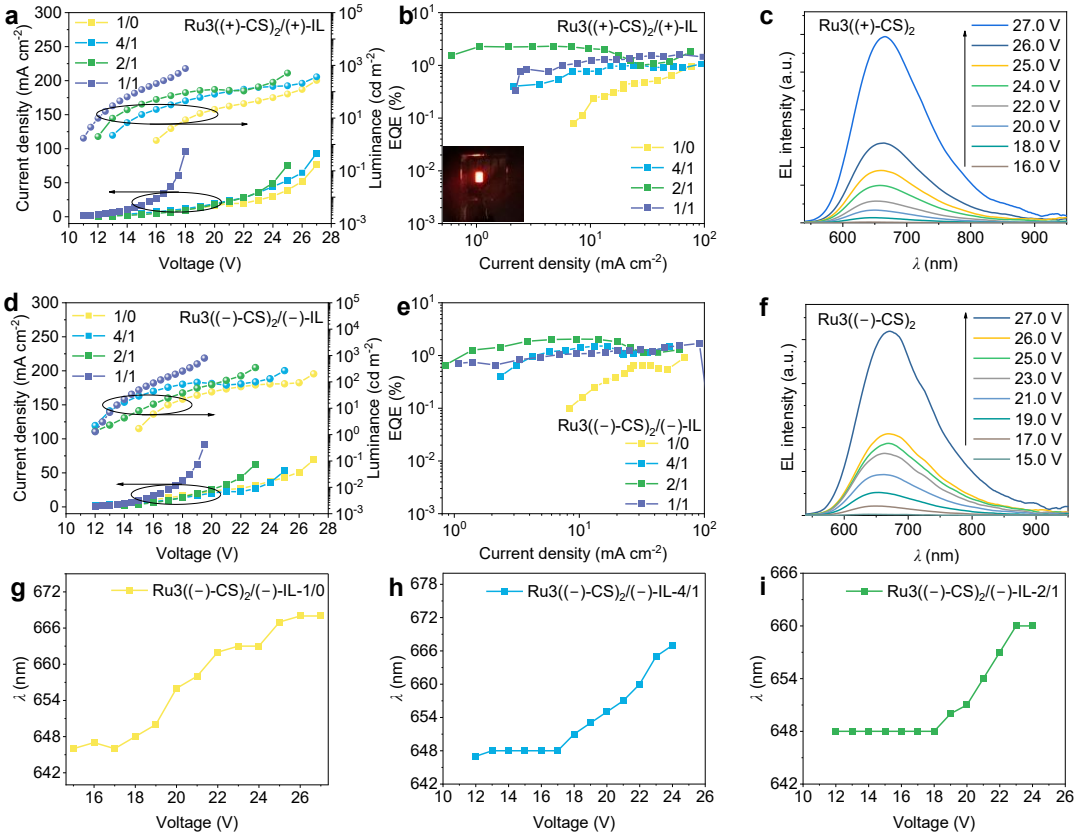

Fig. S20 Device performances of LECs based on mixed Ru3((+)-CS)$_2$/(+)-IL or mixed Ru3((−)-CS)$_2$/(−)-IL with various molar ratios of Ru3((+)/(−)-CS)$_2$ vs (+)/(−)-IL. (a, d) current density-voltage-luminance curves; (b, e) EQE-current density curves; (c, f) EL spectra of (a–c) Ru3((+)-CS)$_2$ and (d–f) Ru3((−)-CS)$_2$ in the absence or presence of chiral ILs (the molar ratios of iTMCs/IL are indicated). (g–i) The corresponding EL peak wavelength as a function of applied voltage. The insets of panel (b) display the image of corresponding LECs in the presence of IL.

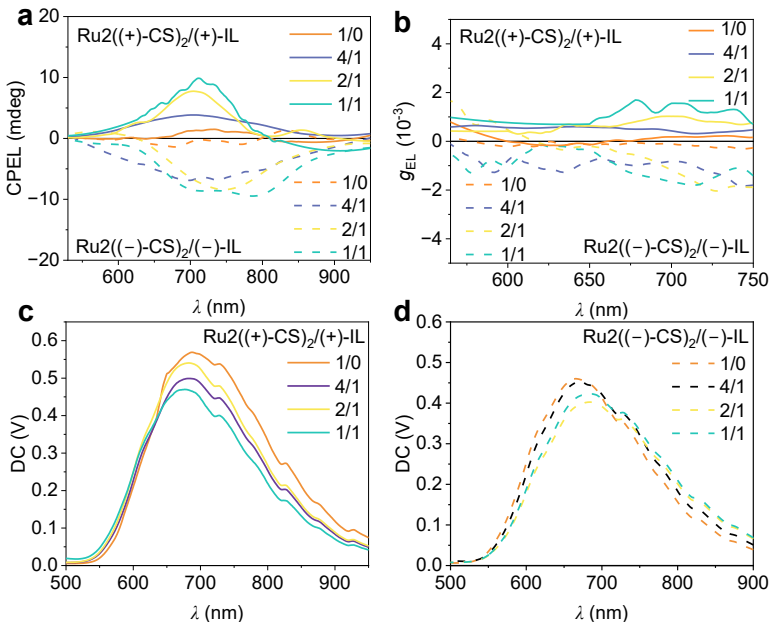

Fig. S21 CPEL performance of pristine and optimized CP-LECs with chiral ILs. (a) CPEL spectra of the LECs based on mixed Ru2((+)-CS)$_2$/(+)-IL or mixed Ru2((−)-CS)$_2$/(−)-IL with varying molar ratios of Ru2(CS)$_2$ vs IL. (b) g_{EL} versus wavelength of corresponding LECs. (c, d) EL spectra of corresponding CP-LECs.

Table S8. Key EL data of the CP-LECs based on mixed Ru2((+)-CS)$_2$/(+)-IL or mixed Ru2((−)-CS)$_2$/(−)-IL with various molar ratios of Ru2(CS)$_2$ vs IL. The g_{EL} values are expressed as mean ± error from three measurements.

EML	Molar ratio	CE_{max} (cd A^{-1})	L_{max} (cd m^{-2})	PE_{max} (lm W^{-1})	EQE_{max} (%)	λ_{EL}(nm)	g_{EL}
Ru2((+)-CS)$_2$/(+)-IL	1/0	0.03	109.1	0.01	0.12	671	–
	4/1	0.06	193.2	0.02	0.21	663	$+4.7(\pm0.7)\times10^{-4}$
	2/1	0.09	339.2	0.03	0.28	663	$+8.2(\pm0.2)\times10^{-4}$
	1/1	0.30	920.1	0.10	0.81	663	$+1.8(\pm0.3)\times10^{-3}$
Ru2((−)-CS)$_2$/(−)-IL	1/0	0.03	101.5	0.01	0.11	667	–
	4/1	0.06	272.5	0.02	0.18	662	$-9.3(\pm0.5)\times10^{-4}$
	2/1	0.12	410.4	0.03	0.38	662	$-5.0(\pm0.7)\times10^{-4}$
	1/1	0.38	830.0	0.14	1.19	660	$-1.4(\pm0.2)\times10^{-3}$

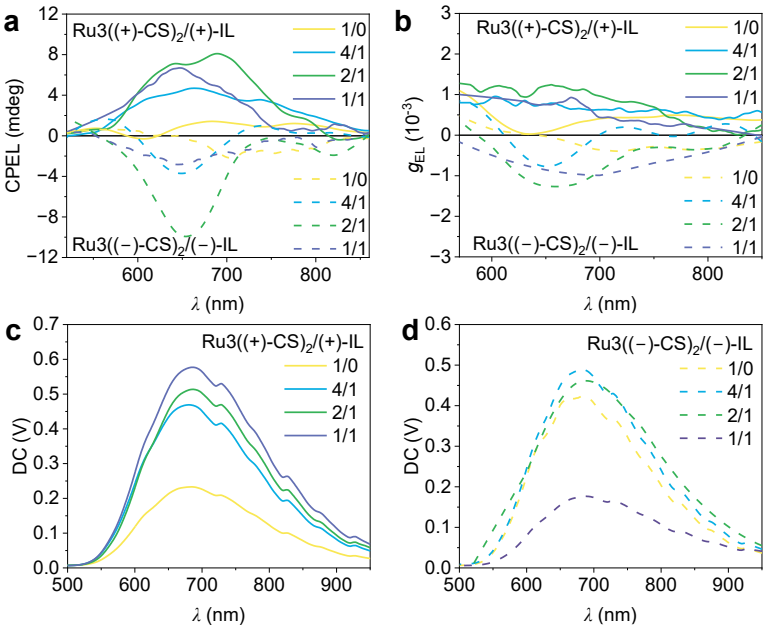

Fig. S22 CPEL performance of pristine and optimized CP-LECs with chiral ILs. (a) CPEL spectra of the LECs based on mixed Ru3((+)-CS)$_2$/(+)-IL or mixed Ru3((−)-CS)$_2$/(−)-IL with varying molar ratios of Ru3(CS)$_2$ vs IL. (b) g_{EL} versus wavelength of corresponding LECs. (c, d) EL spectra of corresponding CP-LECs.

Table S9. Key EL data of the CP-LECs based on mixed Ru3((+)-CS)$_2$/(+)-IL or mixed Ru3((−)-CS)$_2$/(−)-IL with various molar ratios of Ru3(CS)$_2$ vs IL. The g_{EL} values are expressed as mean ± error from three measurements.

EML	Molar ratio	CE_{max} (cd A^{-1})	L_{max} (cd m^{-2})	PE_{max} (lm W^{-1})	EQE_{max} (%)	λ_{EL}(nm)	g_{EL}
Ru3((+)-CS)$_2$/(+)-IL	1/0	0.35	268.7	0.04	0.96	648➞666	+1.4(±0.5) ×10^{-4}
	4/1	0.39	367.4	0.05	1.06	649➞665	+5.9(± 0.4)×10^{-4}
	2/1	1.08	509.5	0.24	2.31	646➞664	+1.4(±0.2) ×10^{-3}
	1/1	0.81	757.1	0.15	1.61	648	+7.1(±1.0) ×10^{-4}
Ru3((−)-CS)$_2$/(−)-IL	1/0	0.29	201.1	0.03	0.91	648➞668	−1.8(±0.6) ×10^{-4}
	4/1	0.50	266.6	0.06	1.51	645➞667	−3.2(± 1.0)×10^{-4}
	2/1	0.93	347.1	0.17	2.01	648➞661	−1.4(±0.2) ×10^{-3}
	1/1	0.87	796.1	0.14	1.70	647	−8.2(±1.0) ×10^{-4}

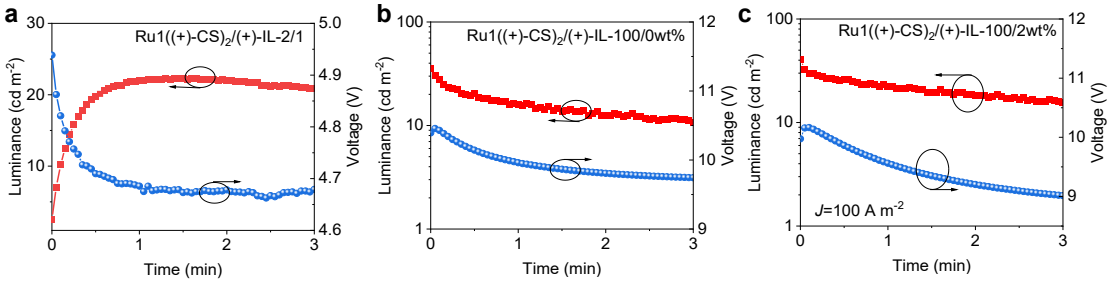

Fig. S23 Time-dependent voltage and luminance characteristics under constant current operation for devices based on Ru1((+)-CS)$_2$. (a) LEC device with a Ru1((+)-CS)$_2$/(+)-IL molar ratio of 2:1. (b) OLED device without IL. (c) IL-containing OLED device with a Ru1((+)-CS)$_2$/(+)-IL weight ratio of 100:2 (wt/wt).

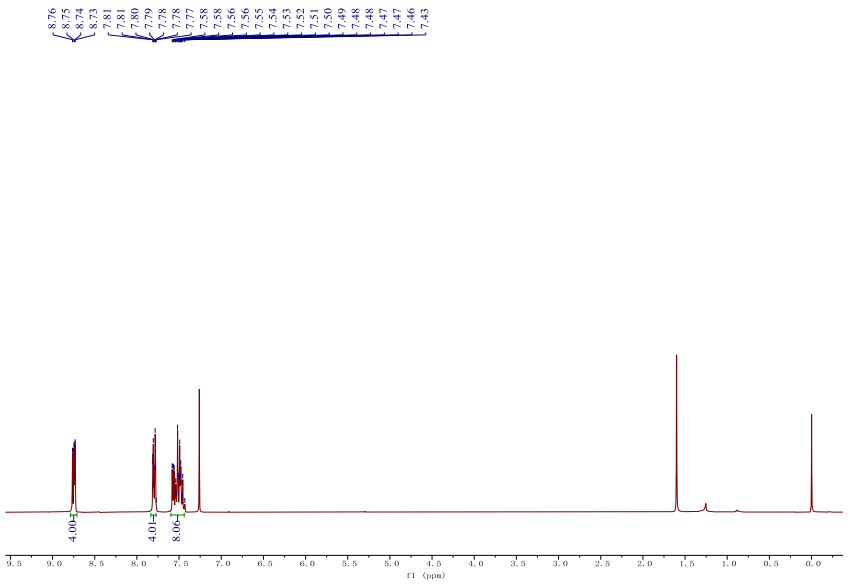

Fig. S24 ^{1}H-NMR spectrum of Ligand2 in $CDCl_3$ solution.

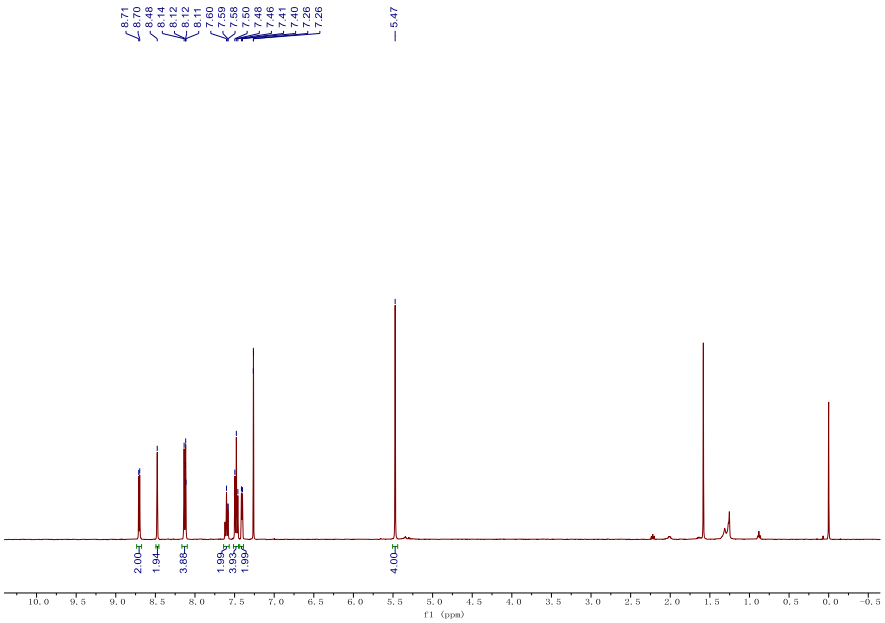

Fig. S25 ^{1}H-NMR spectrum of Ligand3 in $CDCl_3$ solution.

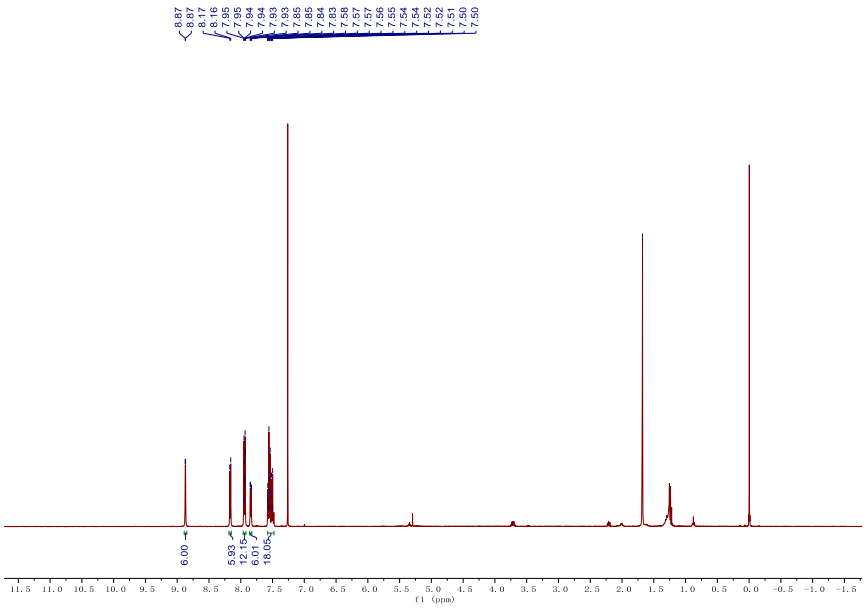

Fig. S26 ^{1}H-NMR spectrum of Ru2 in $CDCl_3$ solution.

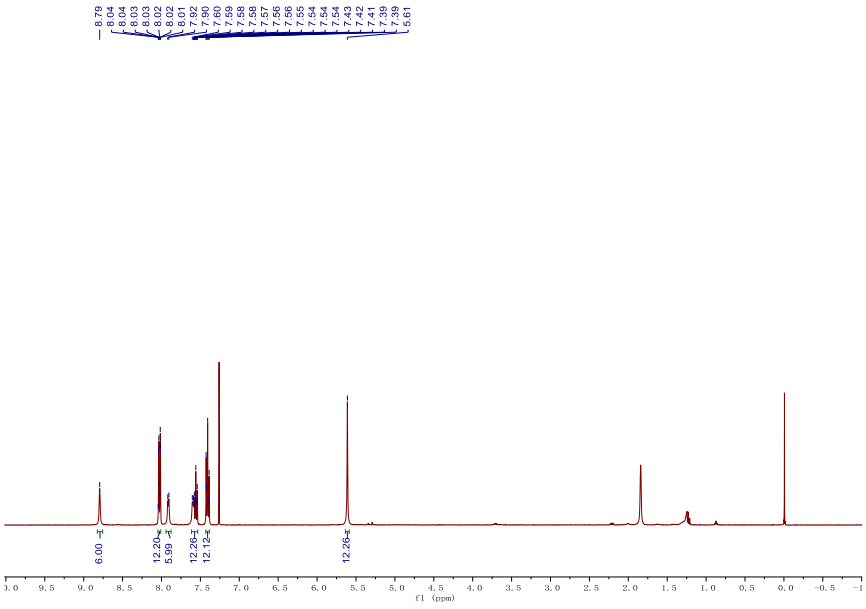

Fig. S27 ^{1}H-NMR spectrum of Ru3 in $CDCl_3$ solution.

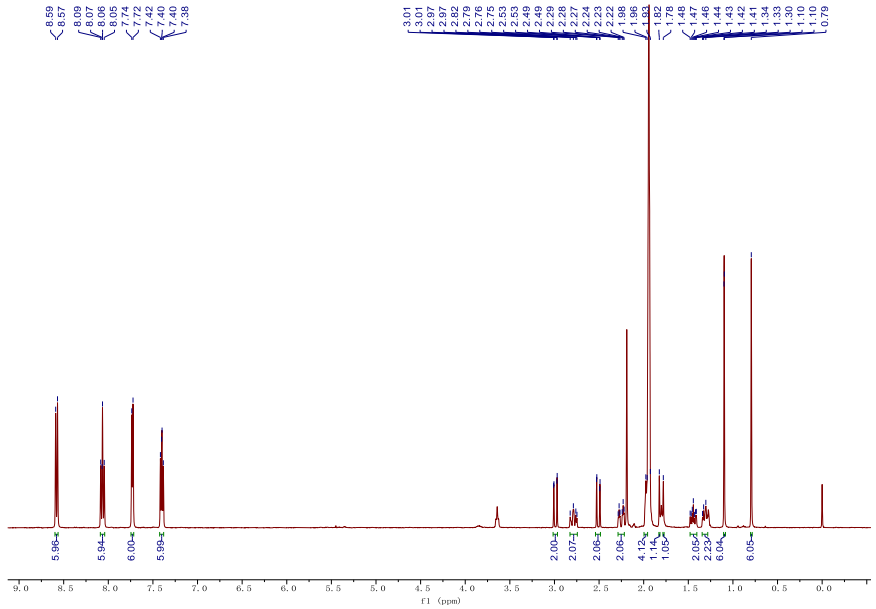

Fig. S28 ^{1}H-NMR spectrum of Ru1((+)-CS)$_2$ in CD_3CN solution.

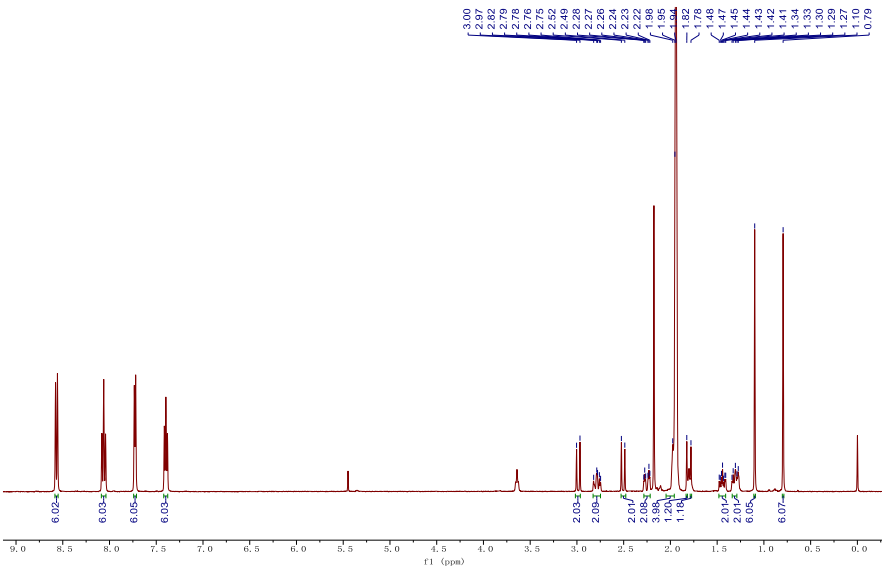

Fig. S29 ^{1}H-NMR spectrum of Ru1((−)-CS)$_2$ in CD_3CN solution.

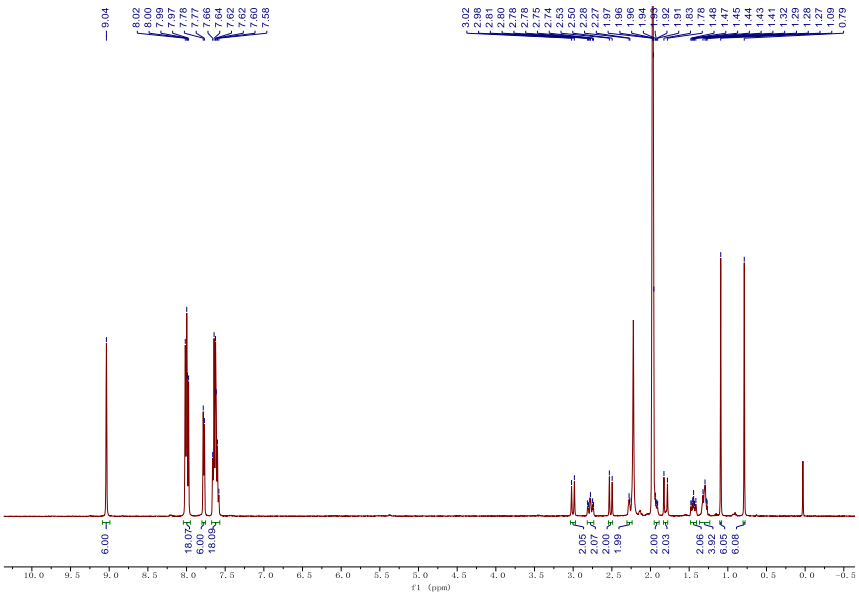

Fig. S30 ^{1}H-NMR spectrum of Ru2((+)-CS)$_2$ in CD_3CN solution.

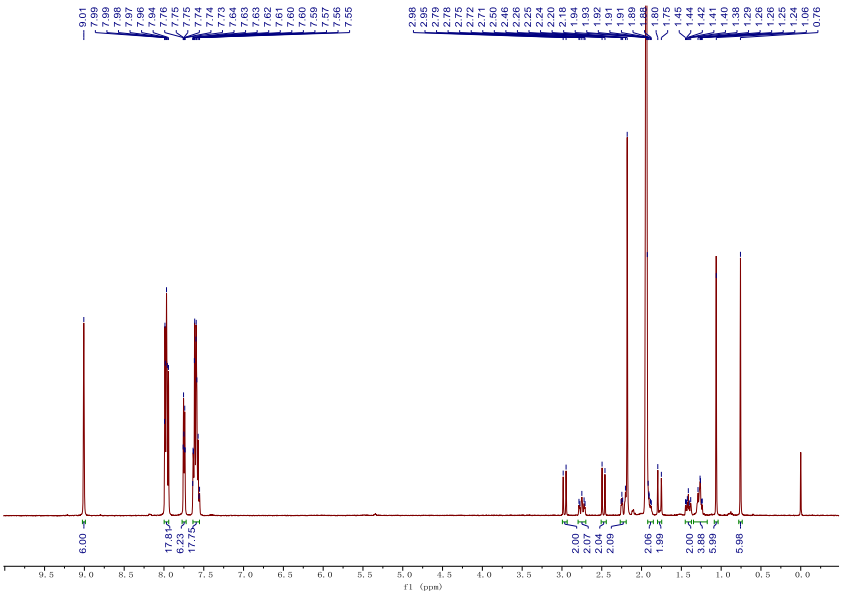

Fig. S31 ^{1}H-NMR spectrum of Ru2((−)-CS)$_2$ in CD_3CN solution.

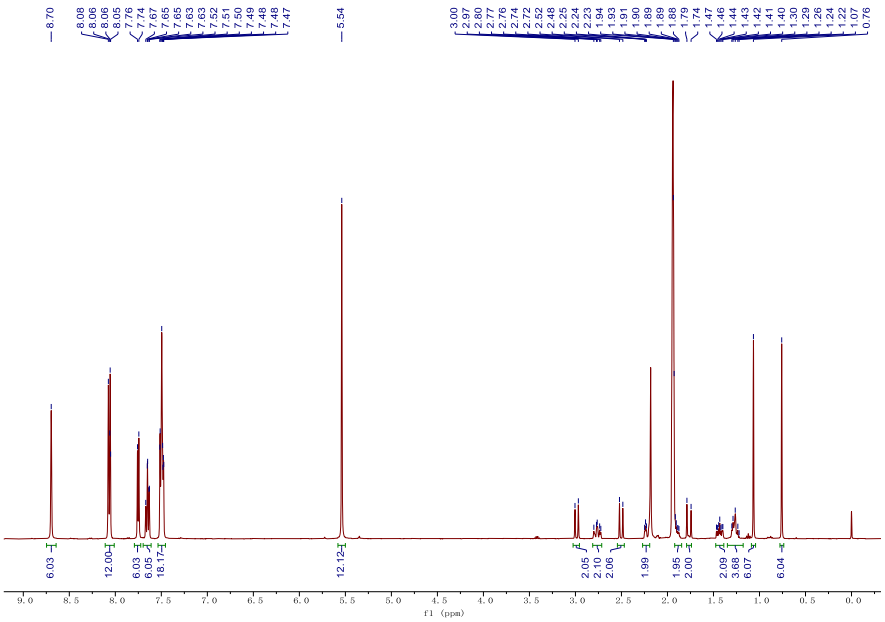

Fig. S32 ^{1}H-NMR spectrum of Ru3((+)-CS)$_2$ in CD_3CN solution.

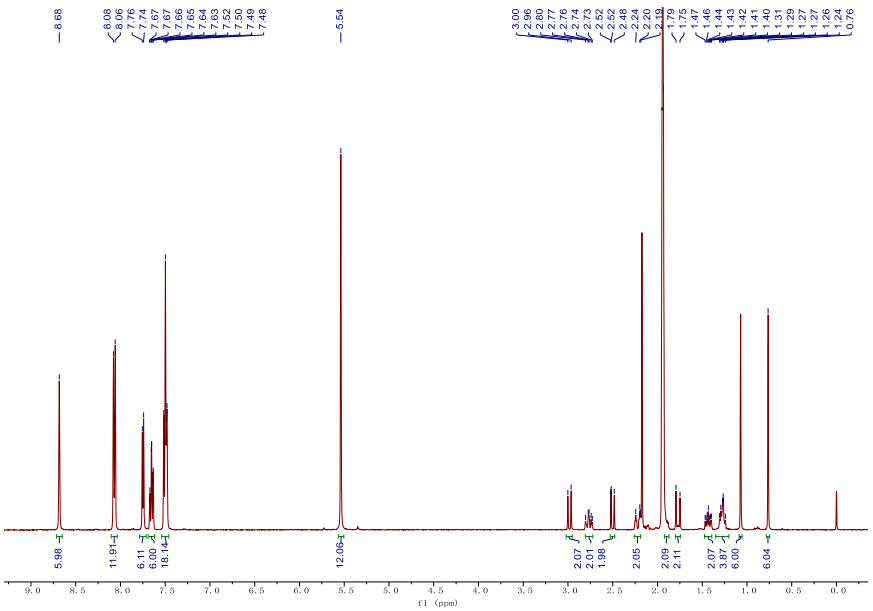

Fig. S33 ^{1}H-NMR spectrum of Ru3((−)-CS)$_2$ in CD_3CN solution.

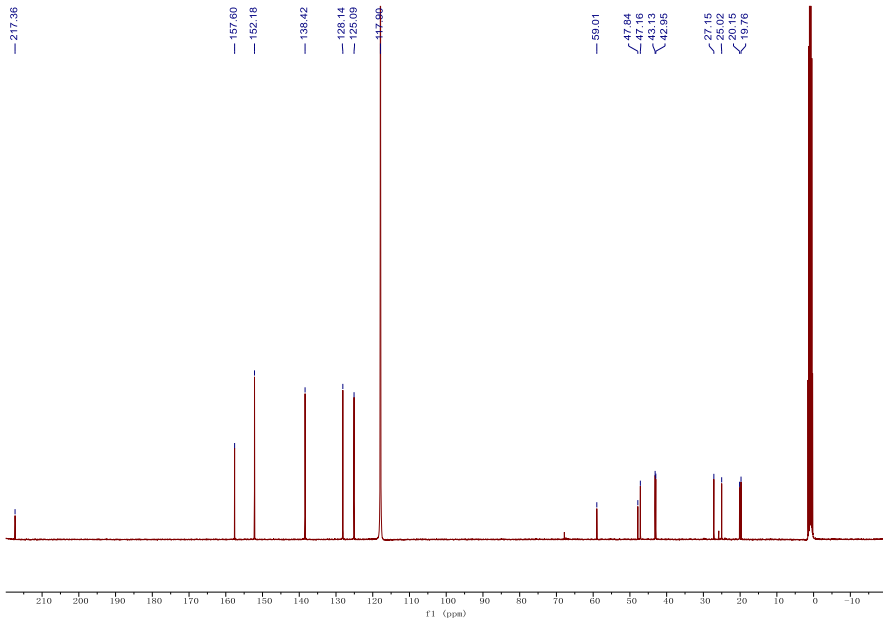

Fig. S34 ^{13}C-NMR spectrum of Ru1((+)-CS)$_2$ in CD_3CN solution.

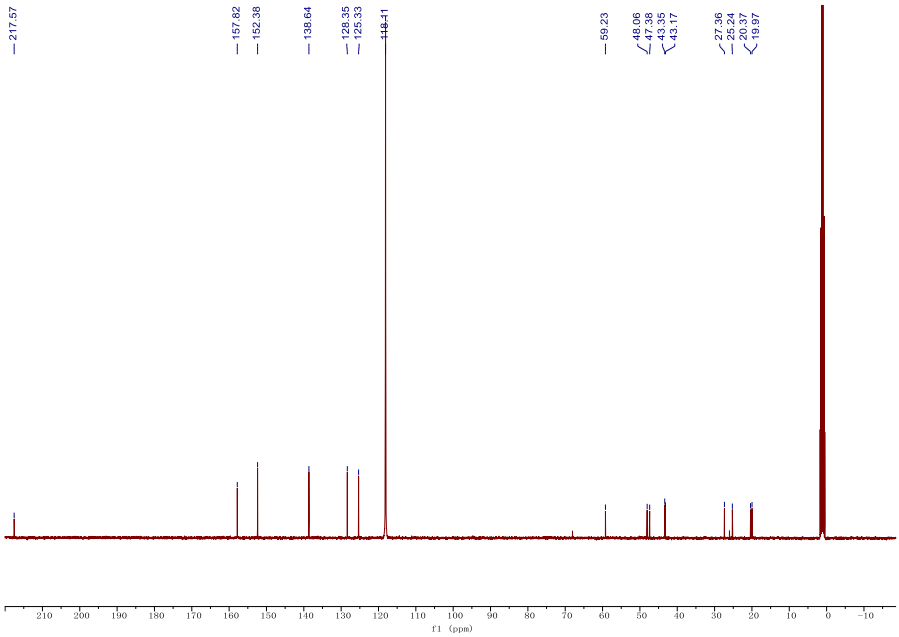

Fig. S35 ^{13}C-NMR spectrum of Ru1((−)-CS)$_2$ in CD_3CN solution.

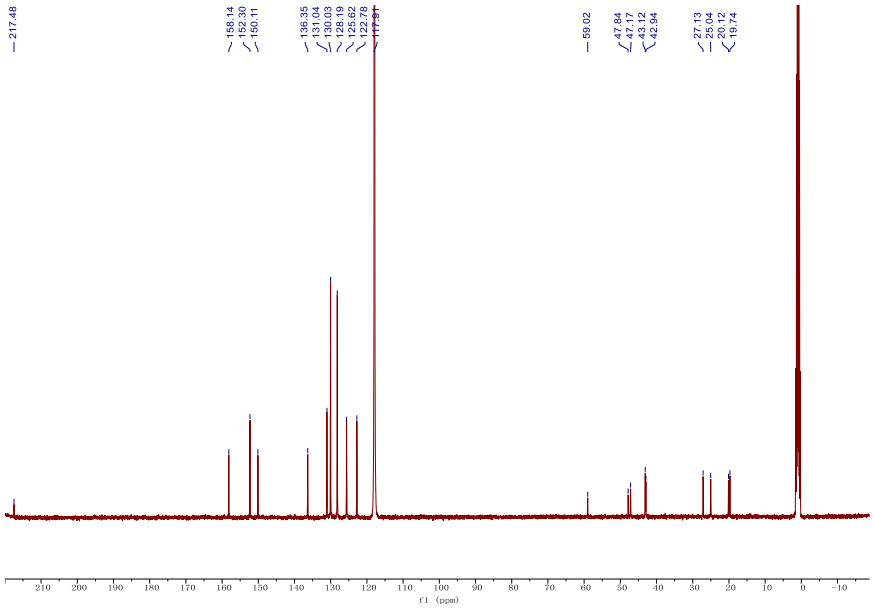

Fig. S36 ^{13}C-NMR spectrum of Ru2((+)-CS)$_2$ in CD_3CN solution.

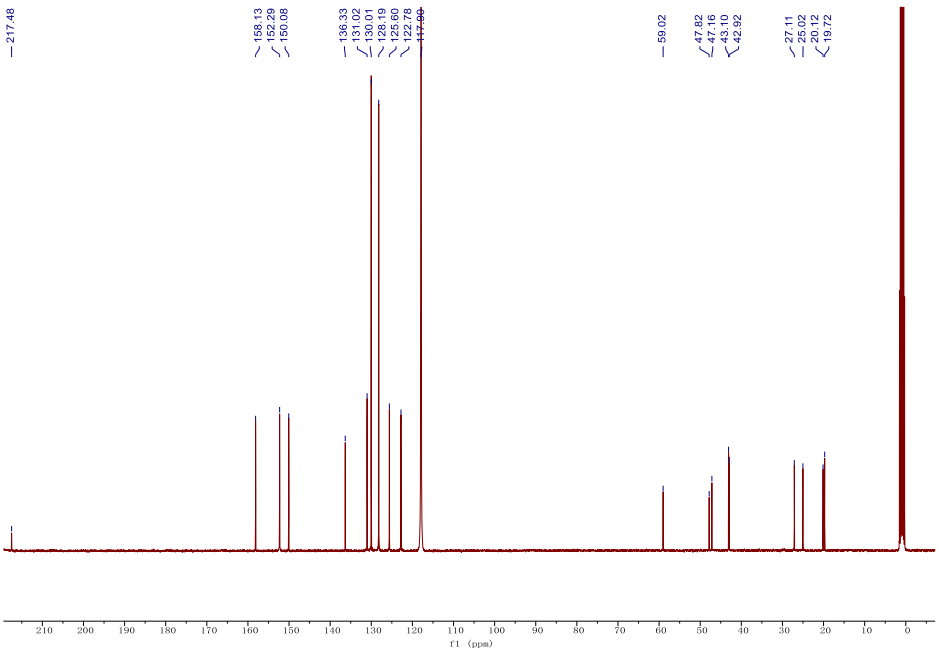

Fig. S37 ^{13}C-NMR spectrum of Ru2((−)-CS)$_2$ in CD_3CN solution.

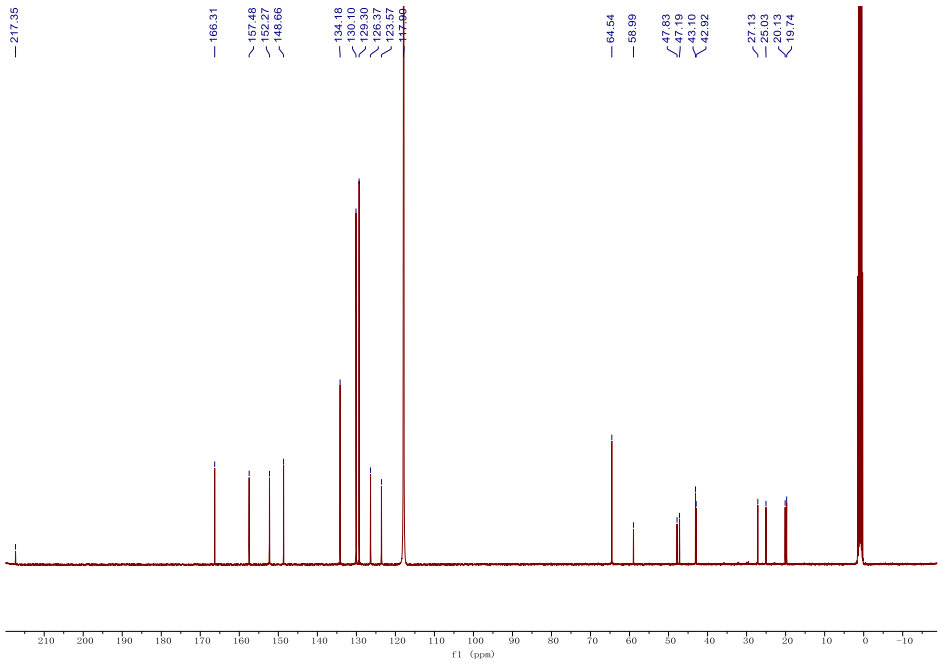

Fig. S38 ^{13}C-NMR spectrum of Ru3((+)-CS)$_2$ in CD_3CN solution.

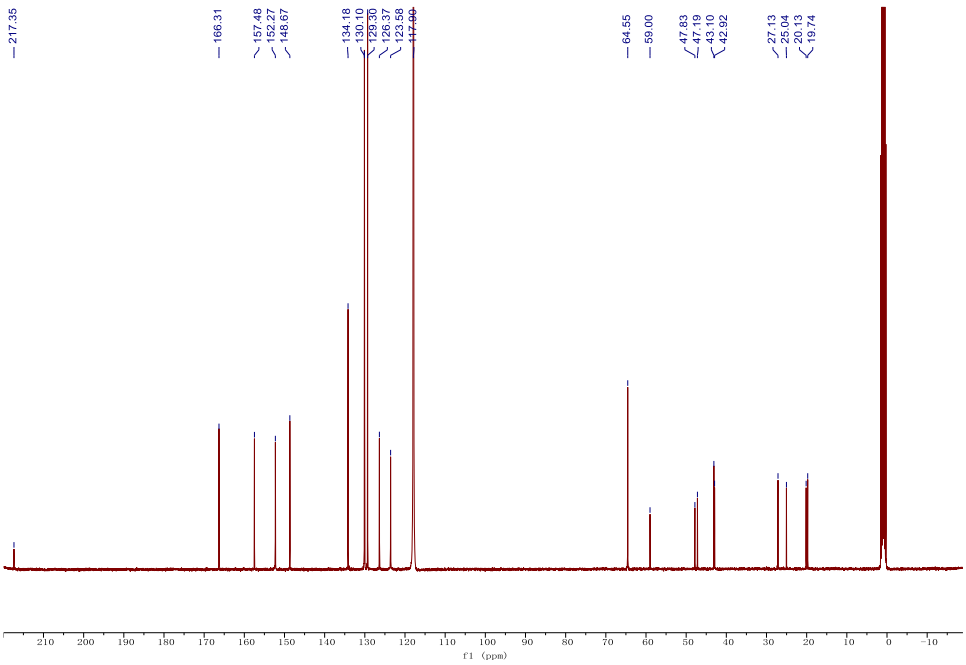

Fig. S39 ^{13}C-NMR spectrum of Ru3((−)-CS)$_2$ in CD_3CN solution.

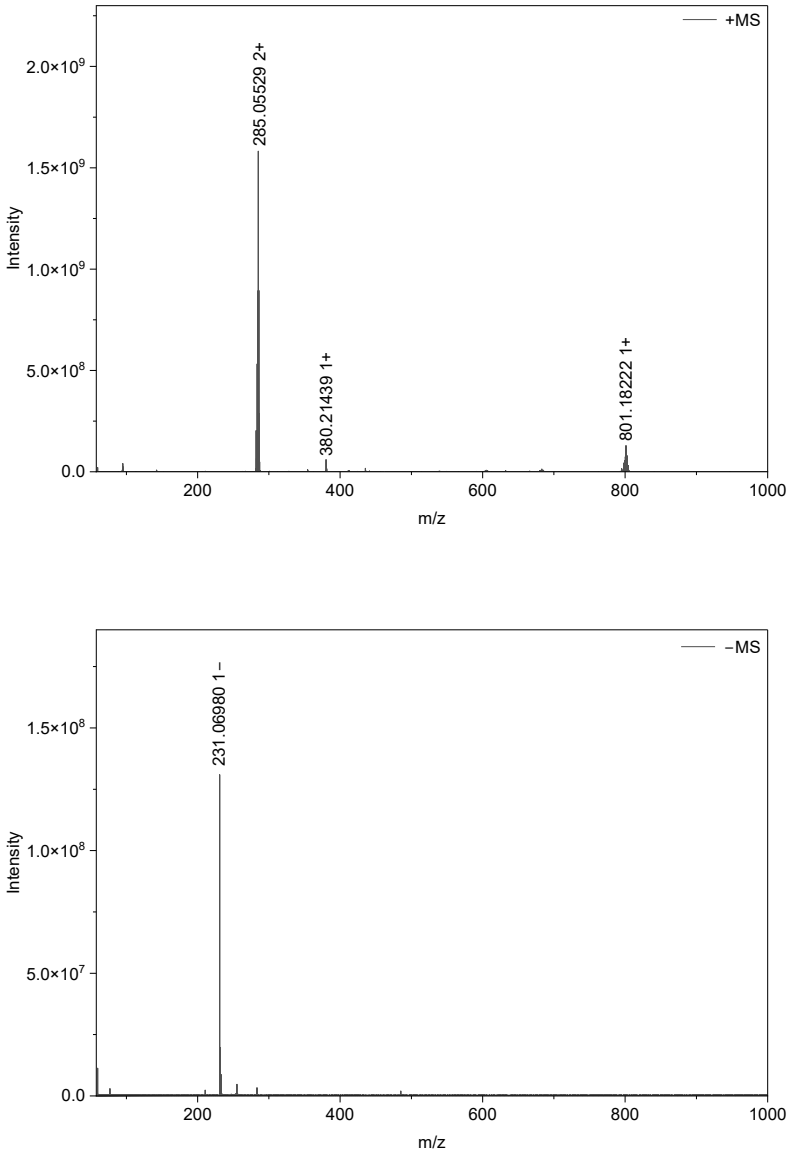

Fig. S40 High-resolution mass spectrum of Ru1((+)-CS)$_2$.

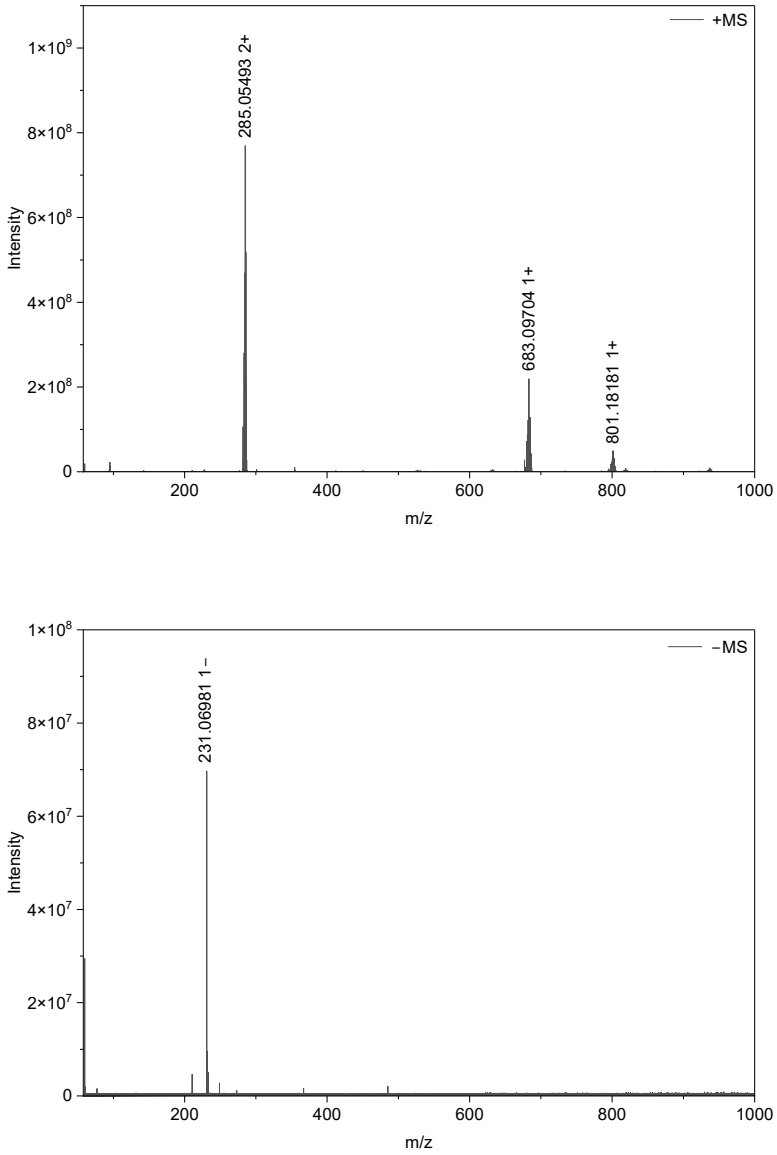

Fig. S41 High-resolution mass spectrum of Ru1((−)-CS)$_2$.

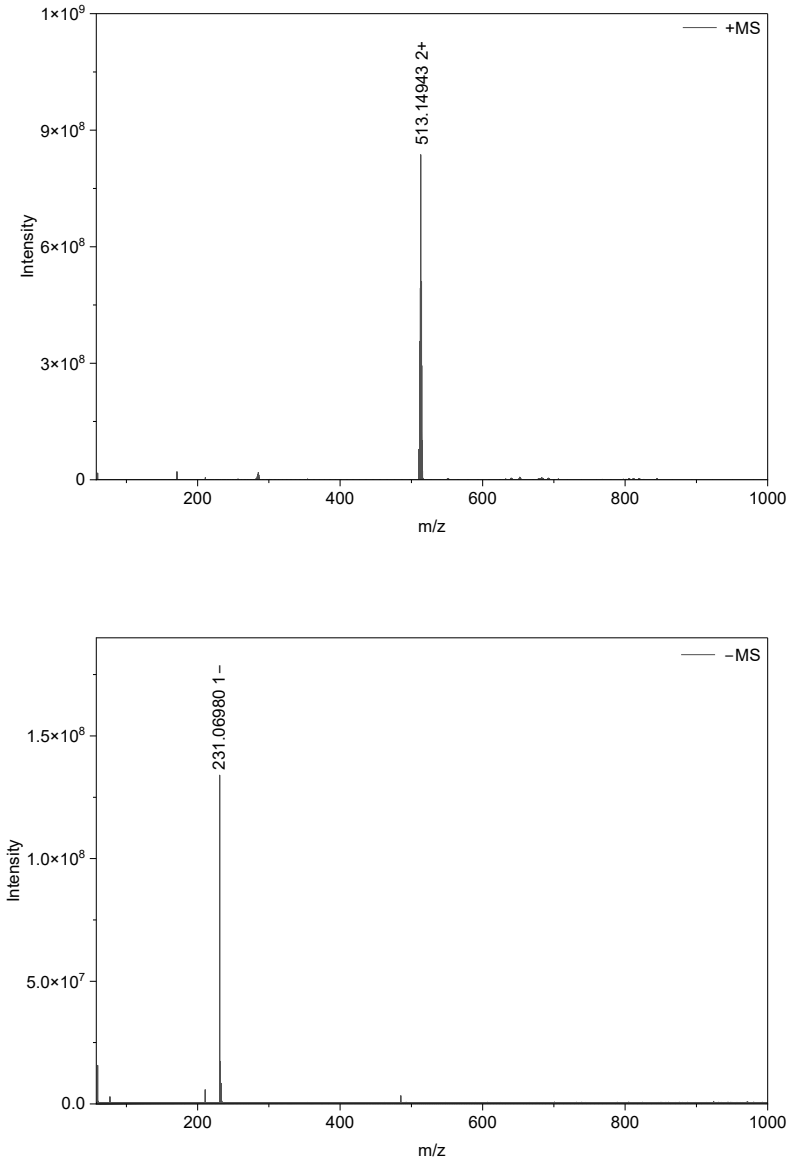

Fig. S42 High-resolution mass spectrum of Ru2((+)-CS)$_2$.

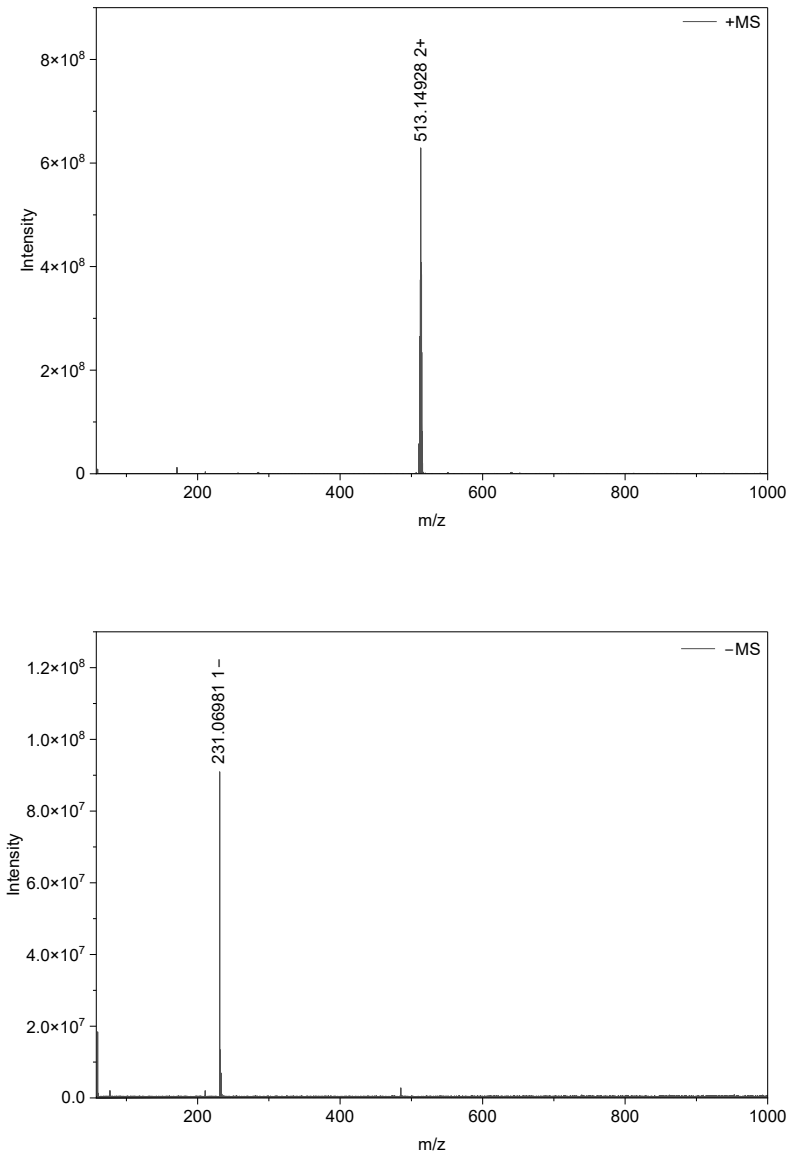

Fig. S43 High-resolution mass spectrum of Ru2((−)-CS)$_2$.

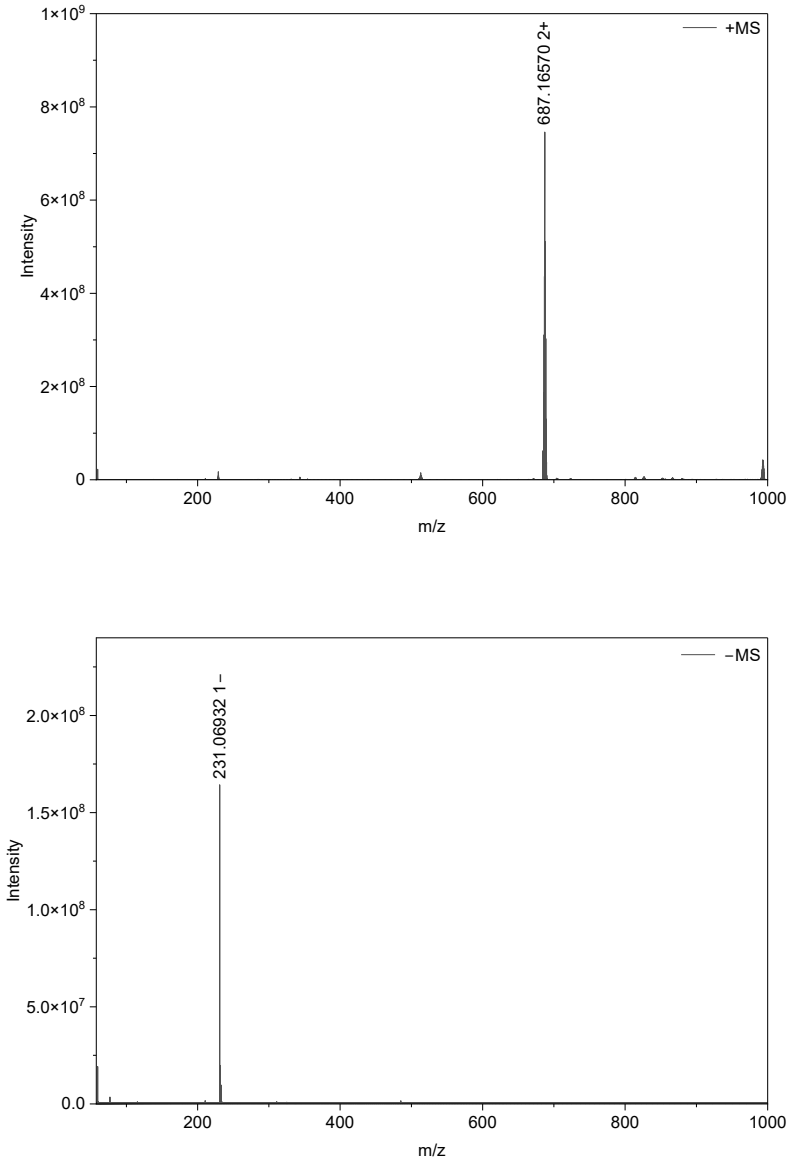

Fig. S44 High-resolution mass spectrum of Ru3((+)-CS)$_2$.

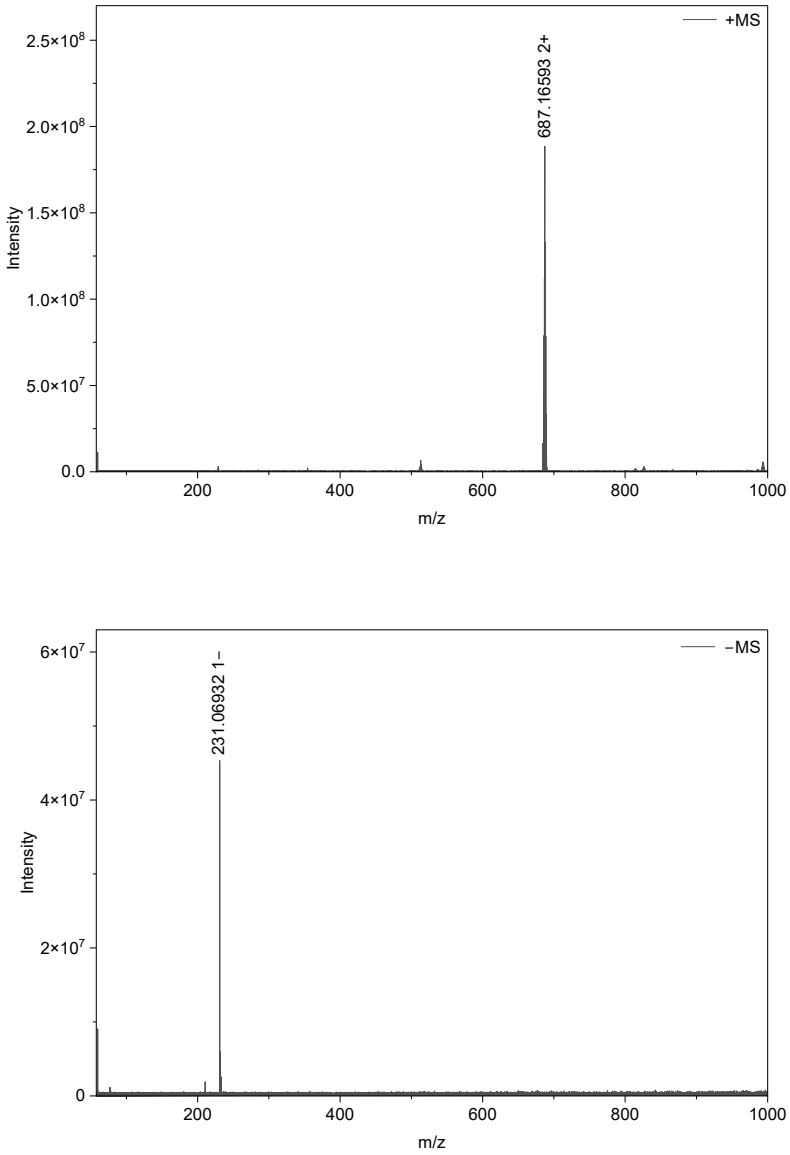

Fig. S45 High-resolution mass spectrum of Ru3((−)-CS)$_2$.

Reference

1. C. Parella, A. Blanquer, S. Sinha, E. Hümpfner, J. Hernando, E. Mora, X. Fontrodona, Z. Kelemen, C. Nogués, R. Núñez and I. Romero, Developing Photo-Activable Ruthenium(II) Complexes for PDT: Synthesis, Characterization, Photophysical and Biological Studies, *Dyes Pigm.,* 2024, **224**, 111985.
2. L. Yang, X. Chen, K. Ni, Y. Li, J. Wu, W. Chen, Y. Ji, L. Feng, F. Li and D. Chen, Proton-Exchanged Montmorillonite-Mediated Reactions of Hetero-Benzyl Acetates: Application to the Synthesis of Zafirlukast, *Tetrahedron Lett.,* 2020, **61**, 152123.
3. L. Paul, K. Enkhbold, S. Robinson, T. T. Aye, Y. Chung, D. P. Harrison, J. A. Pollock and M. R. Norris, Unravelling the Role of $[Ru(bpy)_2(OH_2)_2]^{2+}$ Complexes in Photo-Activated Chemotherapy, *J. Inorg. Biochem.,* 2022, **235**, 111930.
4. F. G. Gao and A. J. Bard, Solid-State Organic Light-Emitting Diodes Based on Tris(2,2'-Bipyridine)Ruthenium(II) Complexes, *J. Am. Chem. Soc.,* 2000, **122**, 7426–7427.
5. H. Rudmann, S. Shimada and M. F. Rubner, Solid-State Light-Emitting Devices Based on the Tris-Chelated Ruthenium(II) Complex. 4. High-Efficiency Light-Emitting Devices Based on Derivatives of the Tris(2,2'-Bipyridyl)Ruthenium(II) Complex, *J. Am. Chem. Soc.,* 2002, **124**, 4918–4921.
6. S. Xun, J. Zhang, X. Li, D. Ma and Z. Y. Wang, Synthesis and Near-Infrared Luminescent Properties of Some Ruthenium Complexes, *Synth. Met.,* 2008, **158**, 484–488.
7. H. J. Bolink, E. Coronado, R. D. Costa, P. Gaviña, E. Ortí and S. Tatay, Deep-Red-Emitting Electrochemical Cells Based on Heteroleptic Bis-Chelated Ruthenium(II) Complexes, *Inorg. Chem.,* 2009, **48**, 3907–3909.
8. I. Oner, C. Sahin and C. Varlikli, Electroluminescence from Two New Ruthenium(II) Complexes as Phosphorescent Dopant: Positive Effect of Swallow-Tail Bipyridyl Ligand, *Dyes Pigm.,* 2012, **95**, 23–32.
9. B. N. Bideh, C. Roldán-Carmona, H. Shahroosvand and M. K. Nazeeruddin, Ruthenium Phenanthroimidazole Complexes for Near Infrared Light-Emitting Electrochemical Cells, *J. Mater. Chem. C,* 2016, **4**, 9674–9679.
10. H. Shahroosvand, S. Abaspour, B. Pashaei, E. Radicchi, F. De Angelis and F. Bonaccorso, A Ruthenium Tetrazole Complex-Based High Efficiency Near Infrared Light Electrochemical Cell, *Chem. Commun.,* 2017, **53**, 6211–6214.
11. B. N. Bideh and H. Shahroosvand, Influence of a π-Conjugated Bridging Ligand in Light-Emitting Electrochemical Cells (LEECs), *ChemistrySelect,* 2018, **3**, 7226–7230.
12. B. N. Bideh and H. Shahroosvand, A Molecularly Engineered Near-Infrared-Light-Emitting Electrochemical Cell (NIR-LEC), *New J. Chem.,* 2020, **44**, 1881–1887.

13. Z.-Q. Li, Y.-D. Wang, J.-Y. Shao, Z. Zhou, Z.-L. Gong, C. Zhang, J. Yao and Y.-W. Zhong, Electrically Amplified Circularly Polarized Luminescence by a Chiral Anion Strategy, *Angew. Chem., Int. Ed.,* 2023, **62**, e202302160.